UiT

THE ARCTIC
UNIVERSITY
OF NORWAY

Faculty of Science and Technology
Department of Physics and Technology

Target Decomposition of Quad-Polarimetric SAR Images as an Unmixing Problem

—

Daniel Norum Danielsen

EOM-3901 Master thesis in Energy, Climate and Environment 30 SP

June 2019

Abstract

Classic target decomposition methods use scattering space in their approaches. However, the goal for this project is to investigate whether a different approach to retrieve accurate and reliable estimates on the earth composition is possible when using the feature space with covariance matrix-based features.

The approach consists of four steps. Generating multidimensional feature space data from sea ice scenes, extracting endmembers, finding the optimal number of endmembers in the scene and finding the contribution for the endmembers to each of the polarimetric feature pixels in the scene. In order to validate the performance of the approach several validation steps where conducted.

Classification of the endmembers, calculating the average reconstruction error, classification of the scene and studding the abundance coefficients were some of these steps. Also, generation of synthetic data was conducted as an additional review of the approach.

The system in this approach does not take in to account the variability of the polarimetric feature values in the different classes. It also assumes that the pixels are linearly mixed, something they probably not are. As a consequence, the approach is not able to retrieve accurate and reliable estimates on the earth composition for scenes consisting of sea ice. However, the approach gave good results on the synthetic datasets.

Further work and investigation on the approach would include adapting the approach to consider the variability all sea ice data suffers from. Further, the methods considering linear mixing should then be replaced with methods considering nonlinear mixing.

Acknowledgements

Contents

List of Figures

List of Tables

Acronyms

AAE average abundance error

ALOS2 Advanced land observing satellite 2

ANC abundance nonnegative constrain

ARE average reconstruction error

ASC abundance sum constrain

ATGP Automatic target generation procedure

CIRFA Centre for Integrated Remote Sensing and Forecasting for Arctic Operations

DUAL-POL dual polarization

EM electromagnetic

FCLS fully constrained least square

H horizontal

HH Horizontal sent and horizontal received

HV Horizontal sent and vertical received

LS least square

LSMA linear spectral mixture analyses

NCLS non-negativity constrained least square

NFINDR N-finder

OEN Optimal endmember number

PolSAR polarimetric SAR

PPI Pixel purity index

quad-pol quad-polarization

ROI region of interest

SAR synthetic aperture radar

SCLS sum to one constrained least squares

SNR signal to noise

V vertical

VH Vertical sent and horizontal received

VV Vertical sent and vertical received

/1

Introduction

Data regarding the earth surface is highly relevant and will continue to be highly relevant in the future. Many businesses, industries and research projects are dependent on earth surface data. Further, these industries will likely require that the data covers large areas, is frequently updated and is of high-quality. For example, the interest in sea ice has had an extensive increase in the later years. Still, investigating the sea ice in the Arctic is not an easy task. The sheer size of the Arctic is one of the main reasons why this is a challenging thing to do. In addition, the Arctic is remote, hard to access, harsh, mostly cloud-covered and dark for several months of the year.

To deliver high quality data, in situ measurements and optical space-borne sensors will have limited value of usage, especially considering the challenges meet when conducting measurements in the Arctic area. However, space-borne microwave synthetic aperture radar (SAR) sensors are not affected by the challenges mentioned above. The SAR have all-weather, day/night imaging capability since it is an active radar and transmits electromagnetic (EM) radiation at microwave frequencies (Bhattacharya, Blumensath, Mulgrew, & Davies, 2007).

The different SAR instruments uses different acquisition modes when collecting the data/images, often dependent on area of interest. Different acquisition modes vary in resolution and spatial coverage. The resolution and the spatial coverage are dependent on each other. A SAR scene with high spatial resolution will have a low spatial coverage, and vice versa(MDA, 2015). A mode that

can collect a large amount of polarimetric information about the backscattering properties of the targets within the SAR scenes is the quad-polarization (QUAD-POL) SAR mode. In a QUAD-POL scene is the sensor transmitting both horizontal and vertical polarized energy, and receive both horizontal and vertical polarized energy, simultaneously. QUAD-POL SAR data provide information about the contribution from different scattering mechanisms (ESA, 2014b).

When taking a natural image scene will the ground in general consist of randomly distributed targets, which will result in back-scattered signals that are stochastic in nature. Target decomposition models a mixture model. The covariance and coherency matrix are based on the second central moment, which is the variance. Therefore are all target decomposition models, which are using the polarimetric covariance or coherence matrices, based on the second order of statistic. There is an assumption in all target decomposition methods, that the signal associated to each pixel is a result of the interaction between several scattering mechanisms. To obtain a better understanding of what the pixels in the image are representing the aim for this project is to explore a new system for enhancing the characterization of earth surface by means of SAR image analysis.

1.1   Objective and contribution

Classic target decomposition methods use the scattering space. However, this method explores the feature space associated with covariance matrix-based features, which can be computed from the QUAD-POL signals. In order to properly and efficiently do so, several steps had to be taken.

In this new approach will a general feature set, extracted from polarimetric data (covariance matrix), be considered as a linear mixture of the primary ground cover classes in the image scene. In other word, each feature set in the multidimensional QUAD-POL feature space can be written as a combination of the endmembers features. The endmembers for this type of data are characterised as pure pixels. Pure pixels are pixels which are not a combination of scattering from multiple materials in the scene. The data manifold will form a simplex which will be spanned by the pure pixels in the multidimensional polarimetric space. Then, the barycentric coordinates will provide information on the actual composition of each pixel as a linear mixture proportion of the different materials. Hence, by inverting a linear optimization problem, information of the fractional abundance of each endmember in every pixel can be calculated.

In order to extract the pure pixels, the Pixel purity index (PPI), N-finder (NFINDR) and Automatic target generation procedure (ATGP) endmember extraction algorithms will be used and the performance for all of these algorithms will be quantified. The aim of the endmember extraction algorithms is to identify the best feature sets which can be used as basis in the mixture model. One will also develop a linear optimization method to unmix the mixing model, which will quantify the actual contribution of every endmember in each target pixel feature set. In order to get a proper characterization of the ability of this approach in delivering information on the composition of each pixel, a proper interpretation of the extracted endmembers as physical classes will be performed. This is done by considering information coming from ground data corresponding to the image scenes. Also, simulated feature sets will be generated in order to calibrate the abundance estimation. Finally, it will be created an unsupervised method for estimating the optimal number of endmembers to be used to drive the mixture model.

The attention has been focused on sea ice scenes due to the challenges that are provided by this sort of analysis. Sea ice will give a proper address of the use of the proposed approach when different properties of the ice (e.g., thickness) are considered or in a situation where the characteristics of the data can be categorized in classes, whose distribution can be very similar to each other.

1.2 Structure of thesis

The thesis will be divided into eleven chapters, including the introduction.

Chapter 2 reviews some of the most important principles of SAR imaging. The chapter will consist of a presentation of the SAR principle, the electromagnetic field, the radar equation, the radar geometry, frequency, polarization and different scattering mechanisms.

Chapter 3 will mainly cover the theory of mixing models. The focus of the chapter will be on linear mixing models, but non-linear mixing models will also be presented.

Chapter 4 will start with an introduction on the theory of generating multidimensional feature data sets. As the feature sets are generated by the covariance matrix, a further analysis of also this theory will have to be conducted.

Chapter 5 contains the theory about endmembers and the different endmember extraction algorithms which are used in this project.

Chapter 6 introduces the theory behind the new method for estimating the optimal number of endmebers to drive the mixture model.

Chapter 7 cover the steps for deriving the fully constrained least square (FCLS) algorithm. It will also present the steps for unmixing and reconstructing data sets. In order to quantify the performance of the FCLS, this chapter will also introduce the Average reconstruction error and the Average abundance error.

In Chapter 8 a presentation of all the different data used in this project will be conducted together with a discussion on the corresponding ground truth to the data.

Chapter 9 covers and explains the computer simulations and experiments which was done in order to evaluate the performance for the approach this paper present.

Chapter 10 reviews and discuss the most interesting results from the computer simulations and experiments.

Chapter 11 will contain a conclusion of the findings of this thesis.

/ 2

SAR Theory

The SAR principle, SAR geometry and scattering mechanisms are some of the topics which will be presented in this chapter. The topics will also form a basis for the following chapters.

2.1 SAR principle

The SAR instrument is a system belonging to the broad class of radar instruments. The SAR, which is an active sensor, works by transmitting EM microwave pulse towards the earth surface. The SAR-antenna then measure the backscattered response from the surface. The backscattered signal consists of magnitude and phase (complex signal) which are unique signatures that reflects the physical properties of a given surface element. The distance from the antenna to the target on the ground can be calculated by measuring the time elapsed from the EM signal was transmitted until it was received. (ESA, 2014a) (CRISP, 2001b).

Since SAR sensors are active sensors and operate in the microwave region, the transmitted signal can penetrate cloud, most weather conditions and works perfectly without any external illumination. These three properties gives SAR a big advantages working in Arctic-areas (CRISP, 2001b).

SAR sensor can be divided into two main categories. First category is the

mono-static which have both the transmitting and the receiving antennas placed closed to each other in one radar station. The other category is the bi-static radars. In this category are both the transmitting and receiving antennas placed apart from each other (Abid Jamal, 2017).

2.1.1 Electromagnetic field

It is normal to assume a monochromatic plane wave when describing EM waves. This implies that absence of sources, i.e., the propagation medium is free of mobile electric charges. The monochromatic time-space electric field is defined as

$$\mathbf{E}(\mathbf{r}, t) = Re[\mathbf{E}(\mathbf{r})e^{j\omega t}] \tag{2.1}$$

where t is the time, r is the space, $\mathbf{E}(\mathbf{r}) = \mathbf{E}_0 e^{-j\mathbf{k}\mathbf{r}}$ is the complex quantities of the electric field, Re indicate the real part, $\mathbf{k}$ is the wave vector and ω is the angular frequency.

The representation of the electric field in the orthogonal basis $(\hat{x}, \hat{y}, \hat{z})$ is given as

$$\mathbf{E}(z, t) = \begin{bmatrix} E_{0_x} e^{-az} cos(\omega t - kz + \delta_x) \\ E_{0_y} e^{-az} cos(\omega t - kz + \delta_y) \\ 0 \end{bmatrix} \tag{2.2}$$

where $\hat{z}$ is the propagation direction, δ is the phase, and a is the attenuation term in the spatial domain. Since the attenuation term is unrelated to the wave polarization, the medium is assumed to be loss free, which gives

$$\mathbf{E}(z, t) = \begin{bmatrix} E_{0_x} cos(\omega t - kz + \delta_x) \\ E_{0_y} cos(\omega t - kz + \delta_y) \\ 0 \end{bmatrix} \tag{2.3}$$

The electric field is composed of two orthogonal sinusoidal waves at a fixed time $t = t_0$. Three types of polarization are possible. It is the linear, circular and elliptical polarization (Lee & Pottier, 2009, page 32-34).

2.1.2 Radar equation

The radar equation describes the fundamental relation between the characteristic of the radar, the target and the received signal. In order to derive the radar equation, the power density at the scatter (S_g) need to be considered first. It is given as

$$S_g = \frac{P_t G}{4\pi r^2} \tag{2.4}$$

where P_t is the power transmitted from the antenna, G is the gain of the antenna and $\frac{1}{4\pi r^2}$ are representing the power density decreasing over the slant range r. By multiplying the power density with the effective receiving area of the scatterer (A_g), the total power intercepted by the scatterer(P_g) are obtained

$$P_g = S_g A_g \tag{2.5}$$

(ESA, 2019)

As the target radiates the power in different directions from the received power input, the amount of power reflected back towards the radar depends on the cross section (σ). The amount of power which the radar receives (P_r) can therefore be written as

$$P_r = S_g \left(\frac{\sigma}{4\pi r^2}\right) = \frac{P_t G \sigma A_e}{(4\pi)^2 r^4} \tag{2.6}$$

where A_e is the is the effective area of the antenna (Tutorialspoint, n.d.). The radar cross section is given as

$$\sigma = A_g(1 - f)G \tag{2.7}$$

Some of the power received by the scatterer is absorbed in losses in the scatter. f is the fraction absorbed(ESA, 2019).

2.1.3 Radar geometry

The flight path for the SAR is in the azimuth direction. The transmitted pulses are sent in the range direction, and each transmitted pulse will cover an area
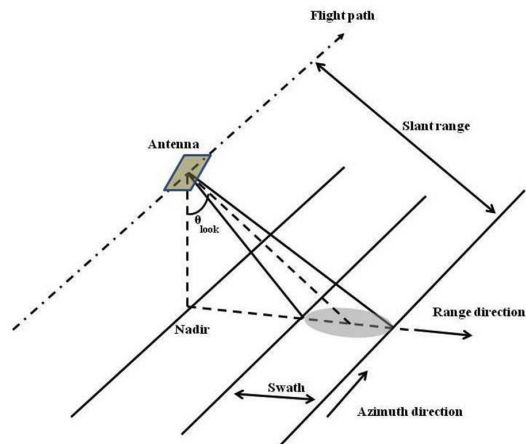
Figure 2.1: SAR image geometry from (Facility, n.d.), Credit: NASA

defined as the antenna beam pattern on the ground. The name for the width of the antenna beam pattern is called the swath width, where the portion of the swath closest to the nadir is called the near range and the portion further away is called the far range. The nadir is defined as the point on the ground located directly under the radar. An angle called the incidence angle (see figure 2.2) will be changed across the swath width. It is defined as the angle between the incident radar signal and the vertical (normal) to the intercepting surface. The look angle is defined as the angle the radar looks at the surface. The angle is given as the angle between the slant range and the nadir. The slant range is the distance measured as a line between the radar antenna and the target (ESA, 2014a). Figure 2.1 and figure 2.2 illustrate some of the radar geometry.

From the recorded backscattered signal, the SAR systems creates a two-dimensional image of the surface. The first dimension is in the range direction and corresponds to the time from when the signal is transmitted and the backscatter signal hits the antenna (ESA, 2014b). The second dimension is in azimuth direction and correspond to the Doppler effect which separates the signals. SAR instruments have a Doppler time delay format. This instrument considers the Doppler history for all the backscattered signals from the target as it moves in azimuth direction. When the satellite moves towards a target, the Doppler effect is high. The doppler effect decreases as the satellite moves away from the target. (ESA, 2014c) (Elachi & Van Zyl, 2006, page 253-255)

Spatial resolution is defined as the finest of details visible in an image. The smaller the distance between two points in an image, the better is the spatial resolution (Campbell & Wynne, 2011). Resolution in range and azimuth direction is defined in two different ways. In the azimuth direction, the spa-
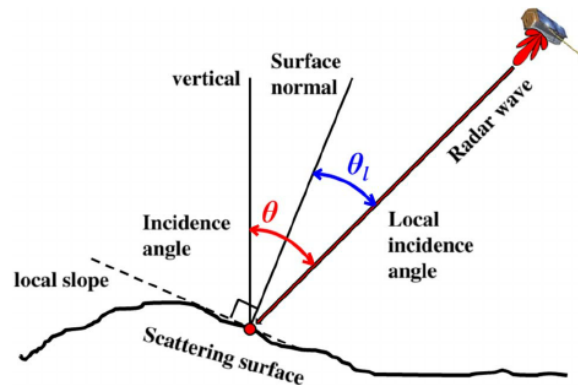
Figure 2.2: Incidence angle. Permission from Professor Paola Rizzoli to use the illustration. The image is from the article(Rizzoli & Brautigam, 2014, page 5977).

tial resolution will be determined by the angular width of the azimuth beam pattern. By keeping track of the history of the Doppler frequency caused by the relative displacement of the target to the antenna, finer azimuth resolution is achieved. The azimuth resolution is equal to half of the antenna length(Chapron, 2012).

$$Resolution = \frac{antenna\ length}{2} \qquad (2.8)$$

Range resolution is defined as the lowest possible time difference between two signals. Signals can only be separated by the sensors if they arrive at different times. Short pulses provides higher resolution (Elachi & Van Zyl, 2006, 239-240).

2.1.4 Frequency

SAR instruments use different microwave bands and the selection of the band is based on the purpose of the mission for the radar. Penetration is the primary factor in wavelength selection. The longer the wavelength is, the greater is the penetration into the target (Podest, 2017). However, a shorter wavelength will better detect roughness. Still, roughness is a relative quantity, simply because weather or not a surface is considered rough, depends on the wavelength. For example can a land surface appear smooth when using a long wavelength radar, because only a small amount of radiation is backscattered from the surface. On the contrary, the same land surface will appear rough when using a short wavelength radar, because large amounts of radiation is backscattered. (CRISP, 2001a)

SAR RADAR Band	Frequency Range(GHz)	Corresponding Wavelength Range(cm)
P	0.230 - 1	130 - 30
L	1 - 2	30 - 15
S	2 - 4	15 - 7.5
C	4 - 8	7.5 - 3.75
X	8 - 12.5	3.75 - 2.40
Ku	12.5 - 18	2.40 - 1.67
K	18 - 26.5	1.67 - 1.13
Ka	26.5 - 40	1.13 -0.75

Table 2.1: Table shows the frequency and wavelength for some of the microwave bands, (USGS, n.d.)

Table 2.1 shows the microwave bands used in radar remote sensing. The Ka-, K-, and Ku-bands are the bands with the smallest wavelength and these bands have some atmospheric opacity. The X-, C-, S-, L-, and P-bands are almost not impacted by the atmosphere (Wikipedia, 2019b). When imaging ocean and ice features is the C band useful. The L band has a longer wavelength and therefore is it more penetrating than the C band. The C band is often utilized in forest and vegetation study as it can penetrate deeper into the vegetation canopy(CRISP, 2001a).

2.1.5   Polarization

Radar polarization is defined as the orientation of the electric field. Traditionally radars have used linear polarization for earth observation. Linear polarization is either vertical (V) or horizontal (H) orientated. Figure 2.3 shows an illustration of linear polarization. The radars can use combinations of the linear polarization when transmitting and receiving polarized energy.

- HV: Horizontal sent and vertical received

- VH: Vertical sent and horizontal received

- VV: Vertical sent and vertical received

- HH: Horizontal sent and horizontal received

The HH and VV combination of received and transmitted polarization energy is said to be like-polarised, while the HV and VH combination is said to be cross-polarised. The description of dual polarization (DUAL-POL) is that the radar can transmit one polarization, and receive both the horizontal and vertical
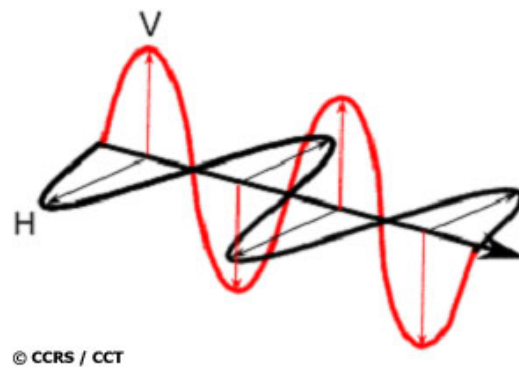
Figure 2.3: Horizontal and vertical polarization image from (Natural Resources Canada, 2015)

return signals, simultaneously.

- VV/VH

- HH/HV

The definition of QUAD-POL is that the radar transmits both horizontal and vertical polarized energy, and receive both horizontal and vertical polarized energy, simultaneously.

- HH, HV, VH and VV.

Scenes achieved using QUAD-POL, will carry more details on backscattering mechanisms than the DUAL-POL scenes do. However, DUAL-POL will achieve larger scenes than QUAD-POL (ESA, 2014b).

2.2   Scattering mechanism

The backscatter signal which the radar receive is a result dependent on several factors. These factors are physical size of the scatterers in the target area, surface roughness, incidence angle, target's electrical properties, wavelength and polarisation of the SAR pulses, observation angles and moisture content (ESA, 2009). In the following sections of this chapter, the three basic types of scattering mechanisms which are prominent in polarimetric SAR (POLSAR) images will be presented. They are defined as the single bounce-, the double bounce- and volume scattering.

2.2.1   Single bounce scattering

The single bounce scattering is when the incident wave only interacts once with the surface boundary. This is normal for surfaces that are smooth and flat relative to the wavelength of the incident wave (Maitra, Gartley, Faulring, & Kerekes, 2013). The incident angle equals the angle of reflection, and therefore the refracted wave will be following Snell's law. Snell's law combines the transmission angle to the incident angle with a refractive index n. Snell's law is given as

$$n_1 sin(\theta_i) = n_2 sin(\theta_r) \tag{2.9}$$

The refractive index n is given by Maxwell's relation as the square root of the dielectric constant (Elachi & Van Zyl, 2006, page 116).

$$n = \sqrt{\epsilon} \tag{2.10}$$

The complex dielectric constant $\underline{\varepsilon}$ describes the electrical properties of a medium, and is given as

$$\underline{\varepsilon} = \varepsilon' - j\varepsilon'' \tag{2.11}$$

(Lee & Pottier, 2009, page 32).

The direction of scattering depends on the surface roughness. The properties of the backscattering can be divided into two components. For a perfectly smooth surface there will be zero return scattering because all the reflected wave is scattered away from the sensor. When the surface is very rough (compared to the incident wave) the result will be a diffuse scattering component(NASDA, 1996a). The surface will backscatter in a Lambertian fashion. It will then have the same amount of scattering in all direction, meaning that the brightness to an observer is the same regardless of the observer's angle of view (Wikipedia, 2019a). The backscatter will in this situation be independent on the incident angle (NASDA, 1996a).

Smooth bare soil and water bodies such as lakes, rivers and oceans demonstrate single bounce scattering (Maitra, Gartley, Faulring, & Kerekes, 2013).

2.2.2 Double bounce scattering

Double bounce scattering is caused by the incident wave interacting with two surfaces, whereas one flat surface is horizontal to an adjacent vertical surface, resulting in a major portion of the transmitted energy being scattered back towards the radar. Double bounce scattering is typically occurring in urban areas with buildings and other vertical structures (Maitra et al., 2013).

For both single- and double bounce scattering, there will be no depolarization of the incident wave on a perfectly smooth surface. The above entails that if an incident wave with a polarization, interacts with a target, the scattered energy will retain the polarization of the incident wave and no response will be created in the cross-pol channel. Looking at phase differences, single bounce and double bounce scatter will not be sharing the same result. The expected phase difference for single-bounce scattering is 0 degree, whilst for double-bounce scattering, the expected phase difference will be ±180 degree (Research, n.d.).

2.2.3 Volume scattering

The last type of scattering mechanism to be discussed is the volume scattering. This type of scattering occurs within inhomogeneous bulk materials that contains local variations in dielectric properties. Volume scattering requires significant penetration of the wave into the medium. But the penetration depth does not only depend on the wavelength. It also depend on the dielectric properties (Elachi & Van Zyl, 2006, page 142). Penetration depth is defined as the depth at which the intensity of the radiation inside the medium falls to $1/e$ of its original value (Jelínková, 2013). Large dielectric constant for the scattering material will result in low- or non-volume scattering. (Puschner, n.d.).

When the incident wave undergoes volume scattering, the received signal may be completely depolarized. Volume scattering results in different phase values uniformly distributed from -180 to $+180$ degree. Examples on materials where volume scattering occur are trees or branches, subsurface or soil layers and snow layers (NASDA, 1996b).

/3

Mixing Models

In order to retrieve accurate and reliable estimates on the earth composition, the approach in this thesis uses a method for unmixing the mixed pixels. To get a better understanding on why this approach uses a unmixing method, it is sensible to have an understanding of what mixed pixels are, how they occur and the challenges that comes with them. Consequently, this chapter will start off with a presentation on facts concerning mixed pixels. We will then move on to mixing models, both linear and nonlinear, in order to get a better understanding of both scenarios.

3.1 Mixed pixels

When subdividing a scene into discrete pixels, the intensity measured by the sensor is averaged over the entire pixel area. If a uniform land area occupies a pixel, then the similar intensity value is averaged and the resulting averaged intensity value forms a responsible representation of the intensity within the pixel. However, some pixels are not occupied by a single homogeneous material, and these different materials differ greatly with respect to intensity measured by a sensor. The average intensity pixel value is then composed by several different values, which result in an averaged pixel value that do not represent any of the material present in the pixel area. Figure 3.1 shows how mixed pixels occurs in a landscape with two different materials (Campbell & Wynne, 2011).
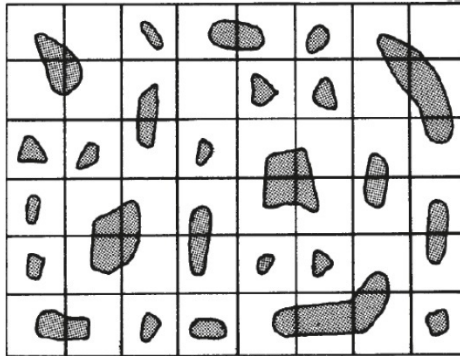
Figure 3.1: Image shows several pixels which are mixed as they contains two different materials. Using the illustration from (Campbell & Wynne, 2011, page 292), with permission from Professor James B. Campbell

3.2   Mixing models

A mixing model is a description of how the combination of endmembers are forming the mixed pixel vector measured by the sensor. Endmembers are defined as unique signatures of the materials in a dataset. Chapter 5 will consist of a deeper description of the endmember and some methods for finding them. The parametrize in a mixing model is the the abundances, which is the contribution of each endmember to a measured pixel value (Dobigeon et al., 2014). Mixing models can be seperated into two different types: linear mixing models and nonlinear mixing models.

3.2.1   Linear mixing models

Linear mixing models holds when assuming that the mixing scale is macroscopic and the incident radiation from the SAR interacts with only one material. The mixing then occurs within the instrument itself because the resolution of the instrument is not fine enough (Bioucas-Dias et al., 2012). Figure 3.2 illustrate how linear mixing can occur.
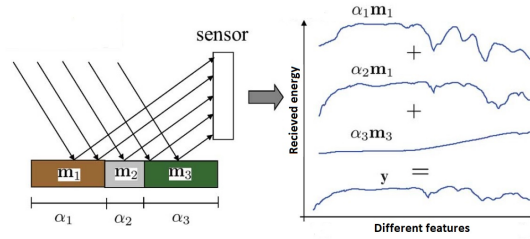
Figure 3.2: Linear mixing.The measured energy at a pixel is a weighted average of the scattered energy of the materials presented in the image. The illustration is a modified version of figure 2 in the article (Bioucas-Dias et al., 2012). The original image was a illustration for linear mixing using optical remote sensing. The illustration is modified in order to fit the description of linear mixing using SAR and a multidimensional feature space.

Given a data set $\mathbf{Y} = [\mathbf{y}_1, ..., \mathbf{y}_N] \in R^{L \times N}$ containing N L-dimensional pixel vectors. The linear mixing model for a given pixel vector, denoted by $\mathbf{y}_p$, can be expressed as

$$\mathbf{y}_p = \sum_{r=1}^{R} \alpha_{r,p} \mathbf{m}_r + \mathbf{n}_p \qquad (3.1)$$

where p denote the given pixel, R is the total number of endmembers in the dataset, $\mathbf{m}_r$ is the signatures of the rth endmember, $\alpha_{r,p}$ is the abundance for the rth endmember and n_p denote an additive perturbation(e.g., noise and modelling error). In (Hapke, 2012) is it stated that the abundances in a linear mixing model represent the relative area of the corresponding endmember imaged region. It is then natural to consider some additional constraints regarding the abundance coefficients $\alpha_{r,p}$

$$\begin{cases} \alpha_{r,p} \geq 0, & \forall p, \ \forall r \\ \sum_{r=1}^{R} \alpha_{r,p} = 1, & \forall p \end{cases} \qquad (3.2)$$

(Dobigeon et al., 2014)

The nonnegativety constraint and the sum to one constraint are often termed abundance nonnegative constrain (ANC) and abundance sum constrain (ASC). Sometimes may researchers expect that the abundance fractions sum to less than one. The reason for that is because an algorithm which calculate the abundance may not be able to account for every material in a pixel. Whether it is better to relax the constraint or to simply consider that part of the modeling error is not clear. (Bioucas-Dias et al., 2012)

3.2.2   Nonlinear mixing models

When one of the two assumptions for linear mixing is not for filled, different nonlinear effects may occur. It is normal to divide the nonlinear models into two families, intimate mixture and bilinear models.

Intimate mixture

The materials are said to be intimately mixed when the interactions occur at a microscopic level, meaning that the materials are in close proximity. These types of image scenes can for example be composed of sand or mineral mixing. Figure 3.3 illustrate intimate mixture. Defining a mixing scale can offer some challenges, as the first requirement of having a microscopic mixing scale is related to the definition of endmembers. Let us consider a scene composed of three materials A,B and C. The retrieval of these three components individually when analysing the scene would be a natural thing to expect. But in other circumstances, one may be interested in the components of the materials themselves, e.g. A_1, A_2, B_1, B_2, C_1 and C_2, assuming that each material is composed of two components. When doing unmixing one might also be interested in all six of the components. Or conversely, maybe it is well known that material A can never present without material B. Unmixing would then consist of identifying the couple A + B and material C.

By associating pure components with individual instances whose resolution have the same order of magnitude as the sensor resolution, the difficulty to define the mixture scale can be circumvented. An example could be considering a patch of sand with spatially homogeneous composition as a unique pure component. In such a case, most of the interactions which occurs in most of the scenes can be assumed to be occurring at a macroscopic level(Dobigeon et al., 2014).

Bilinear models

The other type of nonlinear interaction, called bilinear mixing, occurs at a macroscopic scale in a so-called multi-layered configuration. This kind of nonlinear model will occur when the transmitted radiation is scattered by a material and then reflects off other materials before it reaches the sensor. Scenes covering forest areas, will often deal with this type of configuration. Figure 3.4 illustrate this type of scene (Dobigeon et al., 2014).
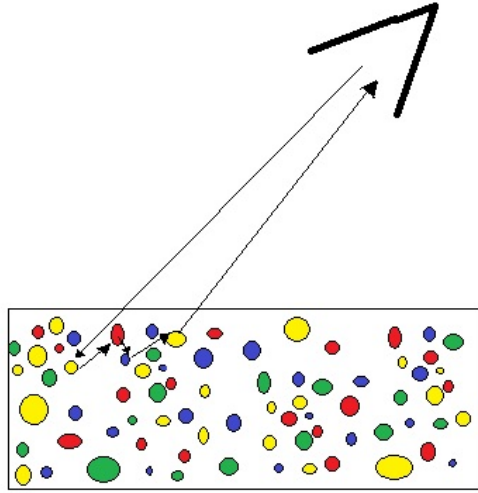
Figure 3.3: Intimate mixture. The figure illustrates how the interactions occurs at a microscopic level.

Many different models have been developed in order to illustrate and to analytically describe these interactions. A simple form of a bilinear model is illustrated bellow.

$$\mathbf{y}_p = \sum_{r=1}^{R} \alpha_{r,p} \mathbf{m}_r + \mathbf{n}_p + \sum_{k=2}^{P} \sum_{r=1}^{R} \beta_{r,k,p} (\mathbf{m}_r)^k \qquad (3.3)$$

The first term in the right-hand side of the equation summarizes the linear contribution. This term is also found in equation 3.1. The second term in the equation summarizes the nonlinear contributions. The coefficient $\beta_{r,k,p}$ adjusts the amount of nonlinearities for the endmembers. Now, three constrains must be considered for the abundances.

$$\begin{cases} \alpha_{r,p} \geq 0, & \forall p, \forall r \\ \beta_{r,k,p} \geq 0, & \forall p, \forall r, \forall k \\ \sum_{r=1}^{R} \alpha_{r,p} + \sum_{k=2}^{P} \sum_{r=1}^{R} \beta_{r,k,p} = 1, & \forall p, \forall k \end{cases} \qquad (3.4)$$

(Dobigeon et al., 2014)

Interpreting the abundances in the bilinear mixing models can be difficult. The bilinear interactions term can form a considerable part of the spectral signal. Accordingly, the linear part of the model will no longer sum to one, which make it difficult to find the total abundance of any given endmember. The
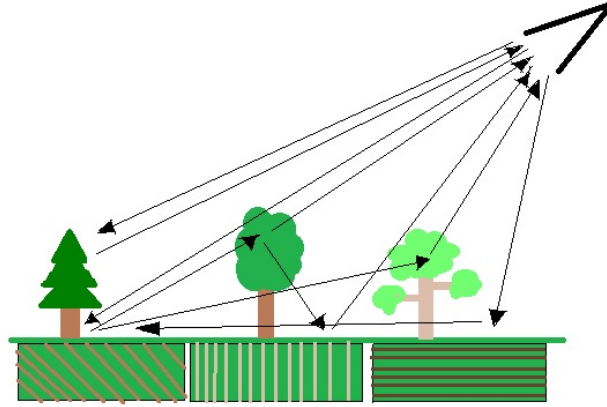
Figure 3.4: Multilayered scene. The radiation scattered from a material is reflected by several other materials before reaching the sensor.

linear and nonlinear abundance coefficients are modelled to sum to one and therefore are the actual areal proportions of each endmember not only given by the linear abundance coefficients. A proposed distribution of the bilinear abundance contribution over the linear abundance coefficient is given as

$$\alpha'_r = \alpha_r + \tau_r \Big(\sum_{k=1}^{r-1} \beta_{k,r} + \sum_{k=r+1}^{R} \beta_{r,k} \Big) \qquad (3.5)$$

where τ is a weighting factor. The corrected abundance α'_r consist of two terms. First term is the linear abundance coefficient. The second term are all the bilinear abundance terms that involves endmember r. The second term is weighted with a scaling factor τ_r. Several values are considered for τ_r. One of the factors is to evenly distribute the bilinear abundance contribution over all R endmembers. This weighting factor is given as

$$\tau_r = 1/R \qquad (3.6)$$

(Heylen, Parente, & Gader, 2014)

4

Feature Generation

The approach in this thesis will use the feature space associated with covariance matrix-based features in order to retrieve information on earth composition. The covariance matrix-based features are stacked upon each other, which results in a data cube, or in other words a multidimensional feature space. Figure 4.1 shows a illustrative example of a multidimensional feature space.

This chapter will review how different covariance matrix-based features can be extracted from QUAD-POL SAR-data in order to create a multidimensional feature space.

4.1 Amplitude and phase difference

QUAD-POL SAR-data consist of complex numbers,

$$a + ib$$

where a and b are real numbers, and "i" is a imaginary number (Çetin & Karl, 2001). By using euler formula, the complex number can be written in the form

$$z = |z|e^{i\theta} \ ,$$

where $|z|$ is known as the complex modulus and θ is known as the phase (wolfram, n.d.).
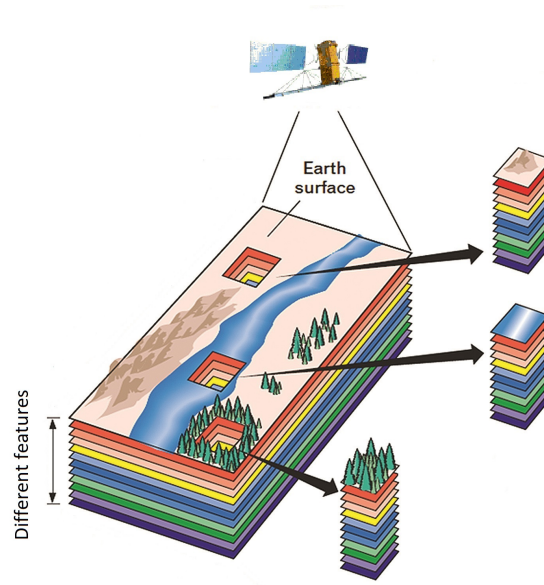
Figure 4.1: Multidimensional feature space. Modified version of the illustration from (Harris, 2018). The original image was an illustration for a multi/hyper-spectral datacube from optical remote sensing. The illustration now fits the description of a multidimensional feature space using SAR.

4.2   Covariance matrix

The complex backscattering metrics relates to the incident and scattered electric field. Another way to show the backscattered signal is by using the covariance matrix (Esmaeilzade, Jahani, & Amini, 2017). It represents the intensity from the scattered radiation dependent on the different polarization.

$$\mathbf{C} = \langle \mathbf{k}_L \cdot \mathbf{k}_L \rangle$$

where $\bar{k}_L$ is the Lexicographic target vector given as

$$\mathbf{k}_L = \begin{bmatrix} S_{hh} \\ S_x \\ S_{vv} \end{bmatrix}$$

S_{HH} and S_{VV} is the like-polarised SAR-data. S_x is a replacement for the the cross-pol SAR-data. This is used if reciprocity is assumed. S_x is given as

$$S_x = \frac{1}{\sqrt{2}}(S_{HV} + S_{VH})$$

When knowing this, the covariance matrix is given as

$$\mathbf{C} = \langle \mathbf{k}_L \mathbf{k}_L \rangle = \begin{bmatrix} \langle S_{HH}S_{HH}* \rangle & \langle S_{HH}S_x* \rangle & \langle S_{HH}S_{VV}* \rangle \\ \langle S_x S_{HH}* \rangle & \langle S_x S_x* \rangle & \langle S_x S_{VV}* \rangle \\ \langle S_{VV}S_{HH}* \rangle & \langle S_{VV}S_x* \rangle & \langle S_{VV}S_{VV}* \rangle \end{bmatrix}$$

4.3 Covariance matrix-based features

This subsection covers mathematical equations in order to extract the covariance matrix-based features. These features together with the diagonals of the covariance matrix are well suited features for target decomposition of sea ice.

- **Determinant of the sample covariance matrix:**

$det(\mathbf{C})$

where $det(\mathbf{C})$ is the determinant of the covariance matrix

- **Eigenvalues of the sample covariance matrix:**

$\lambda_1 > \lambda_2 > \lambda_3$

where λ is the eigenvalues. λ_1 is the biggest and λ_3 the smallest.

- **Polarization fraction:**

$PF = 1 - \frac{\lambda_3}{\lambda_1 + \lambda_2 + \lambda_3}$

where PF is the Polarization fraction.

- **Pedestal height:**

$PH = \frac{\lambda_3}{\lambda_1}$

where PH is the Pedestal height

(Danielsen, 2018)

5

Endmember Extraction

The second step of the approach is to extract the endmembers. The aim of the endmember extraction is to identify the optimal feature sets to be used as basis in the mixture model. For the approach to work, the results from the extraction of the endmembers needs to be successful. If the endmember extraction results are poor, the final results using the approach will also be poor.

The following chapter will focus on the theory of endmembers and different endmember extraction algorithms.

5.1 Endmember

By processing intensity and phase of POLSAR sensed records, the polarimetric signatures can be computed. In each POLSAR scene, microscopic- and macroscopic-scale interactions occur amongst the materials. By investigating the covariance of POLSAR data, polarimetric features can be obtained.

When the spatial heterogeneity is high, and/or where the distribution of the elements are complex at multiple spatial, polarimetric, and radiometric scales, then the effect will be very apparent in complex scenarios. This often leads to datasets which are characterized by data manifolds which might be non-convex and nonlinear, this makes it impossible for pixel properties to be properly described by a small number of polarimetry features. In other words, dimen-
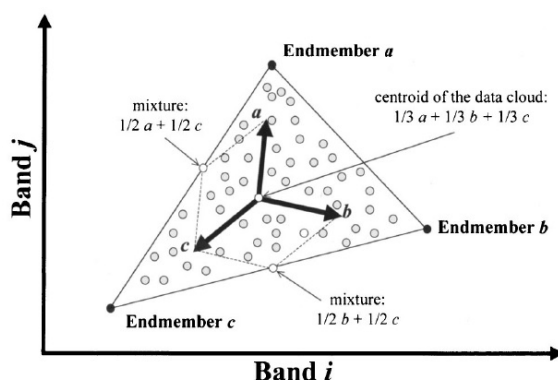
Figure 5.1: Scatterplot of two-dimensional polarimetric feature data illustrating the physical interpretation of a mixture model based on endmembers. Using illustration from Plaza et al. (2002).

sionality reduction will probably lead to loss of information which might will lead to misclassification.

To avoid undesired analysis effects, it is possible to use the high dimensional metric spaces induced by the polarimetric signatures. Each polarimetric signature can be described as a proper combination of the polarimetric signatures, associated with the extremal points, also called endmembers. Endmembers represent a linear basis for the pixel polarimetric signatures, and the coordinates are positive and sum to one. Each polarimetric signature in the multidimensional feature space can be written as a combination of the endmembers signature. Figure 5.1 illustrate a simple mixture model based on three endmembers. The model has the geometrical interpretation of a triangle where the vertices are the endmember and cover fraction is determined by the position of the polarimetric signatures within the triangle (Danielsen, 2018).

In this project, the endmember will function as a unique signature, however, only in regard to the polarimetric signature bands. The rest of this chapter will present three different endmember extraction algorithms. The PPI, ATGP and the NFINDR are all endmember extraction algorithms for linear mixing models. The three applicable algorithms all belongs to the Orthogonal Projection endmember extraction algorithms.

5.2   PPI

Pixel purity index (PPI) is one of the most successful and commonly used approaches for locating appropriate endmembers. The PPI is based on the geometry of convex sets. The pixels are considered as vectors in an N-D space (where N is the number of features bands). First step in the algorithm is a dimensionality reduction on the original data cube by using minimum noise fraction. The next step is to generate several "skewers". Skewers are random N-D vectors. Every pixel is projected into each skewers and the pixel which corresponds to the extrema in the direction of a skewer are identified and placed on a list. One then proceeds to count the number of times a pixel is placed on the list. When all the pixels have been projected into the skewers, the pixels with highest tallies are considered as the purest ones (Danielsen, 2018).

5.3   ATGP

Another approach for endmember extraction is the Automatic target generation procedure (ATGP). The ATGP has the same concept as PPI, which is finding targets of interest in data using orthogonal projections. However, there are still some differences. For example, the PPI requires a very large number of "skewers" to find the maximal/minimal orthogonal projections, as opposed to the ATGP,which uses a sequence of orthogonal subspaces with the maximal orthogonal projections to find the targets of interest. That is the reason why ATGP sequentially extracts targets one at a time.

The ATGP makes use of the orthogonal subspace projector, which is defined as

$$P_{\mathbf{U}}^{\perp} = \mathbf{I} - \mathbf{U}(\mathbf{U}^{\mathbf{T}}\mathbf{U})^{-1}\mathbf{U}^{\mathbf{T}} \tag{5.1}$$

where $\mathbf{I}$ is an identity matrix. By repeatedly using the orthogonal subspace projector, the endmembers in the data is found. The process starts with assuming that $\mathbf{m}_0$ is a initial endmember pixel vector. Sets $\mathbf{U} = \mathbf{m}_0$ and apply an orthogonal subspace projector $P_{\mathbf{m}_0}^{\perp}$ to all the image pixels vectors ($\mathbf{r}$). The endmember pixel vector $\mathbf{m}_1$ is then found by setting n=1 and use the equation:

$$\mathrm{m}_n = \arg\left\{\max_{\mathrm{r}}\left[\left(P_{\mathbf{U}_{n-1}}^{\perp}\mathbf{r}\right)^{T}\left(P_{\mathbf{U}_{n-1}}^{\perp}\mathbf{r}\right)\right]\right\} \tag{5.2}$$

Then $\mathbf{m}_2$ can be found by setting $\mathbf{U} = [\mathbf{m}_0\mathbf{m}_1]$ and repeat the above procedure. The procedure is repeated over and over again to find the endmember pixel

vectors m_3, m_4, *etc*. The procedure will go on until it is stopped by a certain stopping rule. An example on a stopping rule can be that the procedure stops if n < p-1.

The endmember matrix generated at the (n-1) stage is then given as

$$\mathbf{U}_{n-1} = [\mathbf{m}_1 \mathbf{m}_2 ... \mathbf{m}_{n-1}]$$ (5.3)

The endmember matrix is then defined by U_{p-1} and contains p−1 endmebers. U_{p-1} do not include the initial endmember vector $\mathbf{m}_0$ (Danielsen, 2018).

5.4   NFINDR

The N-finder (NFINDR) is the last algorithm to be discussed in relations to endmember extraction. This algorithm finds the set of pixels with the largest possible volume, which is done by inflating a simplex within the data. The full image cube is used as input to the algorithm. Initially a random set of vectors are selected. Every pixel in the image is then evaluated in terms of pixel purity likelihood or nearly pure statehood. This is in order to refine the initial estimate of endmembers. A trial volume is calculated for every pixel in the place of each endmember. If replacement of endmembers with some of the pixels result in an increase in volume, then those pixels will replace the endmembers. This procedure repeats until the endmember can't be replaced (Danielsen, 2018).

6

Optimal Endmember Number

The approach and methods used in this project are unsupervised, meaning that there is no additional data added which can be used to train the algorithms. One part of the missing information is the number of classes in the data. Retrieving such information is very valuable in order obtain information on the earth composition. The third step in the approach is therefore extracting the expected number of classes in the scene.

This chapter will cover the theory of a new method for finding the optimal number of endmembers in a scene. From this point on, the method will be characterized as the Optimal endmember number (OEN).

The data manifold will form a simplex in the multidimensional polarimetric space. The pure pixels, endmembers, will then span the simplex. The volume V of the simplex spanned by the endmembers can be given as

$$(-1)^R 2^{R-1}((R-1)!)^2 V^2 = det(\mathbf{C}_{1,2,\dots R}) \tag{6.1}$$

and it can be calculated in terms of the inter-vertex distances using the Cayley-

Menger determinant, which is

$$det(\mathbf{C}_{1,2,\ldots R}) \tag{6.2}$$

In these equations are R the total number of endmembers spanning the simplex, and $\mathbf{C}_{1,2,\ldots R}$ is given as

$$\mathbf{C}_{1,2,\ldots R} = \begin{bmatrix} 0 & d_{12}^2 & \cdots & d_{1R}^2 & 1 \\ d_{21}^2 & 0 & \cdots & d_{2R}^2 & 1 \\ \vdots & \vdots & \ddots & \vdots & 1 \\ d_{R1}^2 & d_{R2}^2 & \cdots & 0 & 1 \\ 1 & 1 & \cdots & 1 & 0 \end{bmatrix} \tag{6.3}$$

d_{ij} is given as the Euclidean distance between endmember $\mathbf{x}_i$ and $\mathbf{x}_j$ (Heylen, Burazerovic, & Scheunders, 2011). The Euclidean distance is given as

$$d_{ij} = \sqrt{\sum_{i=1}^{L}(x_i - x_j)^2} \tag{6.4}$$

meaning that the euclidean distance is the square root of the sum of squared differences between corresponding elements of two vectors. If the endmembers in the Cayley-Menger determinant is similar, the $\mathbf{C}_{1,2,\ldots R}$ matrix will contain small numbers, resulting in a small volume (Kersten, Lee, & Ainsworth, 2005).

The optimal number of endmembers is the number of endmembers which gives the largest volume of the simplex. By using the number that gives the largest volume, the chance for having enough endmembers to span the hole data manifold is large. Also, by using the number which gives the largest volume, the chance for over fitting/over training the system is decreased. The system is over fitted when the number of extracted endmembers is at the point where it overcomes the real number of classes in the scene. When this happen, the extracted endmembers are no longer real pure pixels, but instead mixed pixels and/or pixels which are similar to the real pure pixels.

/7

Unmixing

When knowing the number of classes in the scene, which is calculated using the OEN method, the next step in the approach is to unmix the data in order to find the contribution of the classes on each pixel. By successfully do that, allot of information is obtained on the earth composition. Each feature set in the multidimensional feature space can be written as a combination of the endmember features. The fully constrained least square (FCLS) is a method which estimates the fractional endmember abundance coefficient for each pixel feature set, and thereby unmixing the mixed pixels.

The following chapter will focus on the steps for deriving the FCLS algorithms. The chapter will also contain a presentation on how to reconstruct the dataset and use the average reconstruction error and the average abundance error to quantify the performance of the reconstruction and the FCLS.

7.1   FCLS

The FCLS method is a method designed to analyse linear mixture of pixels. The method falls within the category of linear spectral mixture analyses (LSMA) method. These methods, including the FCLS, is originally designed to work on multispectral/hyperspectral data. However, the FCLS method will in this thesis be used to analyse the linear mixture of pixels in POLSAR data, using multidimensional feature space data, not multispectral/hyperspectral

data.

LSMA methods are used to provide an estimation on the abundance fraction on the endmembers contribution to a pixel. In order to provide an accurate and reliable estimate, two constraints must be imposed. These are the ANC and ASC which was introduced in section Linear mixing models. The ASC is easy to implement, as opposed to the ANC. Therefore, many LSMA-based methods are unconstrained. These methods, e.g., minimum distance, maximum likelihood estimation, least square method (LSM), can only provide sub optimal solutions. The estimation of the abundances estimated by the unconstrained LSMA do not generally reflect the true and accurate abundance fraction, and cannot be used for material quantification.

In order to derive the FCLS we need to start with the simple equation 3.1 for a linear mixture model. The equation 3.1 can be rewritten to

$$\mathbf{y}_p = \mathbf{M}\alpha + \mathbf{n} \tag{7.1}$$

where $\mathbf{y}_p$ still is the pixel vector, $\mathbf{M} = [\mathbf{m}_1, \mathbf{m}_2, ..., \mathbf{m}_R]^T$ is a matrix consisting of the endmembers in the PolSAR scene, $\alpha = [\alpha_{1,p}, \alpha_{2,p}, ..., \alpha_{R,p}]^T$ is the abundance coefficients and $\mathbf{n}$ is still denoted as additive perturbation. Linear unmixing methods attempts to unmix the unknown abundance fractions via an inverse of linear mixing model. The linear mixing model represent an unconstrained linear mixing problem. To solve this problem, we will need to look at the Orthogonal Subspace Projection, as it will lead to the FCLS method.

First step in the orthogonal Subspace Projection approach is selecting a single endmember $\mathbf{d}$ from the endmember matrix $\mathbf{M}$. In order to not lose any generality, the selected endmember, which is the desired material signature, is assumed to be $\mathbf{d} = \mathbf{m}_R$. $\mathbf{U} = [\mathbf{m}_1, \mathbf{m}_2, ..., \mathbf{m}_{R-1}]^T$ is then the undesired endmember matrix consisting of the undesired endmembers. Equation 7.1 can then be rewritten as

$$\mathbf{y}_p = \mathbf{d}\alpha_R + \mathbf{U}\gamma + \mathbf{n} \tag{7.2}$$

where γ is the vector consisting of the abundances associated with the undesired endmembers in $\mathbf{U}$ and α_R is the abundance for the desired endmember $\mathbf{d}$ (Heinz et al., 2001). From equation 7.2 it is possible to develop an operator that eliminates the effects of $\mathbf{U}$ and maximizes the remaining signal energy with respect to the noise. In (Harsanyi & Chang, 1994), using equation 7.2, a classification operator for the endmember of interes $\mathbf{d}$ is the derived, resulting in an orthogonal subspace projection operator given as

$$\mathbf{P}_{OSP}(\mathbf{y}_p) = \mathbf{d}^T P_{\mathbf{U}}^{\perp}(\mathbf{y}_p) \tag{7.3}$$

where $P_U^\perp = (\mathbf{I} - \mathbf{U}\mathbf{U}^\#)$ and $\mathbf{U}^\# = (\mathbf{U}\mathbf{U})^{-1}\mathbf{U}^T$. But the orthogonal subspace projection classifier in equation 7.3 is assuming that the abundance α is known, which is not the case. In (Chang, Zhao, Althouse, & Pan, 1998) and (Tu, Chen, & Chang, 1997) are several techniques developed in order to estimate $\alpha = [\alpha_{1,p}, \alpha_{2,p}, ..., \alpha_{R,p}]^T$. These techniques are based on a posteriori information obtained from the image data. From these techniques we get a least square (LS) projection classifier given as

$$\mathbf{P}_{LS}(\mathbf{y}_p) = (\mathbf{d}^T P_U^\perp \mathbf{d})^{-1}\mathbf{P}_{OSP}(\mathbf{y}_p) \tag{7.4}$$

and the least square estimate of α is given as

$$\hat{\alpha}_{LS} = (\mathbf{M}^T\mathbf{M})^{-1}\mathbf{M}^T\mathbf{y}_p \tag{7.5}$$

For finding the fully constrained version of P_{LS}, we need to find the a partially constrained least square. In (Heinz et al., 2001) they refer to (Settle & Drake, 1993) for the deriving of the sum to one constrained least squares (SCLS) method, which is done by imposing of the ASC on α. $\hat{\alpha}_{SCLS}$ is then given as

$$\hat{\alpha}_{SCLS} = \mathbf{P}_{M,1}^\perp \hat{\alpha}_{LS} + (\mathbf{M}^T\mathbf{M})^{-1}\mathbf{1}[\mathbf{1}^T(\mathbf{M}^T\mathbf{M})^{-1}\mathbf{1}]^{-1} \tag{7.6}$$

where $\mathbf{P}_{M,1}^\perp = \mathbf{I} - (\mathbf{M}^T\mathbf{M})^{-1}\mathbf{1}[\mathbf{1}^T(\mathbf{M}^T\mathbf{M})^{-1}\mathbf{1}]^{-1}\mathbf{1}^T$ and $\mathbf{1}$ is a vector consisting of 1 with the length of R, $\mathbf{1} = [1, 1, ..., 1]^T$.

Next, we want to impose the ANC on the linear mixing problem while discarding the ASC. The non-negativity constrained least square (NCLS) method is described by the following optimization problem

Minimize least square error $= (\mathbf{M}\alpha - \mathbf{y}_p)^T(M\alpha - \mathbf{y}_p)$ over α subject to $\alpha \geq 0$
$$\tag{7.7}$$

The least square error is used as the criterion for optimisation. But the constraint $\alpha \geq 0$ is a set of inequalities and therefore are the Lagrange multiplier method not suitable to use for solving the optimal solution. This non-negative constraint problem is solved by using an unknown R-dimensional positive constraint constant vector $\mathbf{c} = [c_1, c_2, ..., c_R]^R$ with $c_j > 0$ for $1 \leq j \leq R$. Now can a Lagrangian J be given as

$$J = \frac{1}{2}(\mathbf{M}\alpha - \mathbf{y}_p)^T(M\alpha - \mathbf{y}_p) + \lambda(\alpha - \mathbf{c}) \tag{7.8}$$

By setting $\alpha = \mathbf{c}$ and then take the partial derivative of J with respect to α, the following is given

$$\frac{\partial J}{\partial \alpha}\bigg|_{\alpha_{NCLS}} = 0 \Rightarrow \mathbf{M}^T \mathbf{M} \hat{\alpha}_{NCLS} - \mathbf{M}^T \mathbf{y}_p + \lambda = 0 \tag{7.9}$$

which gives

$$\hat{\alpha}_{NCLS} = (\mathbf{M}^T \mathbf{M})^{-1} \mathbf{M}^T \mathbf{y}_p - (\mathbf{M}^T \mathbf{M})^{-1} \lambda = \hat{\alpha}_{LS} - (\mathbf{M}^T \mathbf{M})^{-1} \lambda \tag{7.10}$$

The FCLS algorithm is generated by using the NCLS algorithm in conjunction with the ASC. The ASC is included in the endmember matrix $\mathbf{M}$ by introducing a new endmember matrix

$$N = \begin{bmatrix} \delta \mathbf{M} \\ \mathbf{1}^T \end{bmatrix} \tag{7.11}$$

and a vector $\mathbf{s}$ given by

$$s = \begin{bmatrix} \delta \mathbf{y}_p \\ \mathbf{1}^T \end{bmatrix} \tag{7.12}$$

δ in equation 7.11 and 7.12 controls the impact of the ASC. The FCLS algorithm can now be derived directly from the NCLS algorithm by replacing the $\mathbf{M}$ and the $\mathbf{y}_p$ used in the NCLS algorithm with $\mathbf{N}$ and $\mathbf{s}$ (Heinz et al., 2001).

7.2 Data reconstruction and average reconstruction error

Reconstructing the data by using the extracted endmembers and abundance coefficients is a good way to validate if the approach has been successful or not. When knowing both the endmembers and their fractional abundance to each target pixel feature, it is easy to reconstruct the dataset. Based on the equation 3.1 for a linear mixing model, the reconstructed dataset can be calculated using

$$\hat{\mathbf{y}}_p = \sum_{r=1}^{R} \hat{\alpha}_{r,p} \hat{\mathbf{m}}_r \tag{7.13}$$

where p denote the given pixel, R is the total number of endmembers in the dataset, $\hat{\mathbf{m}}_r$ is the signatures of the rth extracted endmember, $\hat{\alpha}_{r,p}$ is the estimated abundance coefficient using FCLS with the endmembers $\mathbf{M} = [\mathbf{m}_1 \mathbf{m}_2 ... \mathbf{m}_R]$.

The accuracy of this reconstruction procedures can be evaluated thanks to the average reconstruction error (ARE), which is defined as

$$ARE = \sqrt{\frac{1}{LN} \sum_{p=1}^{N} \|y_p - \hat{y}_p\|^2}, \tag{7.14}$$

where L is the number of features in the multidimensional feature space data, N is the total number of pixels and y_p is pixel p in the original multidimensional feature space data (Dobigeon et al., 2014).

7.3 Average abundance error

In order to calculate the ability for the FCLS to estimate the abundances coefficients, we take inspiration in ARE equation (7.14). Instead of comparing the reconstructed data with the original data, we calculate the average abundance error (AAE) by comparing the estimated abundances coefficients with the original abundances coefficients. The equation for the AAE will be

$$AAE = \sqrt{\frac{1}{LN} \sum_{p=1}^{N} \|\alpha_{r,p} - \hat{\alpha}_{r,p}\|^2}, \tag{7.15}$$

8

Experimental Data

In this project, three different datasets from three different sensors has been used to test the performance of the approach. All the datasets included different types of ground truth. This chapter will cover information concerning the different datasets and the different ground truths.

8.1 Radarsat-2

The first dataset to be discussed is the dataset stemming from the Radarsat-2 satellite with QUAD-POL mode. This data was collected from a region outside the east of Greenland on the date 31 of July 2016, and the time for the first and last zero doppler azimuth time was 13 : 40 : 33.47 and 13 : 40 : 37.90. Figure 8.1 shows the area where the PolSAR data was collected. The incidence angel range is from 26.162 degree (incidence near) to 29.427 degree (incidence far). The range sampling spacing was 4.733 m and the azimuth sample spacing was 4.803 m. The raster height was 6117 lines and the raster width were 4905 samples. The antenna pointing direction was to the right.

People with vast experience within the filed has advises that the data should be a composition of sea and different types of sea ice. Figure 8.2 shows the RGB colour composite using the multilooked radar cross section for the given scene. In the image are $\langle \sigma_{hh} \rangle = 4\pi C_{11}$ representing red color, $\langle \sigma_x \rangle = 4\pi C_{22}$ representing green color, $\langle \sigma_{vv} \rangle = 4\pi C_{33}$ representing blue color and C is the

covariance matrix.

This Radarsat2 data belongs to an AWI campaign conducted by CIRFA UiT in the summer of 2016. To this campaigne it follows a dataset containing ground truth, which was collected by an EM Bird. The EM Bird measured the thickness of the ice in meters. The ground truth dataset also included the coordinates (latitude and longitude) for the measured ice thickness. The EM Bird started to measure the corresponding scene around seven minutes after the Radarsat2 data was collected. Figure 8.3 shows the flight path for the EM Bird over the Radarsat2 scene.

(a)

(b)
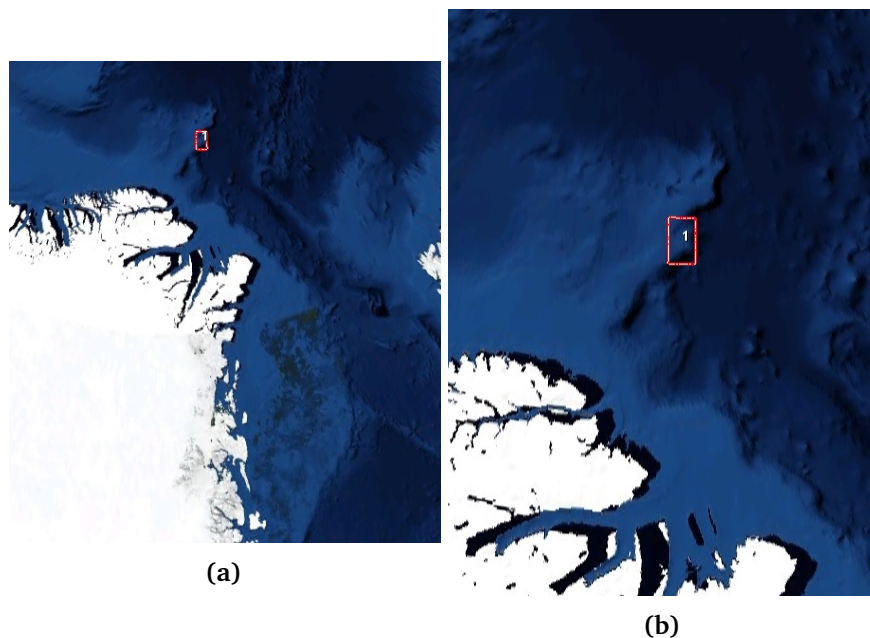
Figure 8.1: Image shows the area where the PolSAR data was collected from Radarsat2. This data was collected from a region outside the east of Greenland. The image is produced using the program SNAP
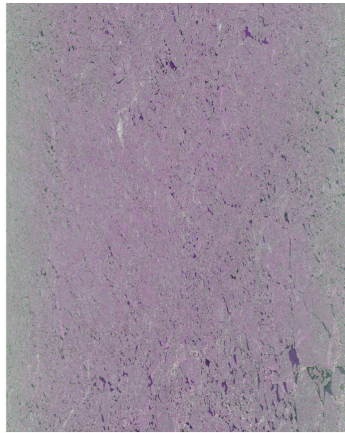
Figure 8.2: RGB colour composite using the multilooked radar cross section

Figure 8.3: Flight path for the EM bird over the Radarsat2 scene. Image is produced by Malin Johansson, Associate Postdoc, UiT. Got permission from her to use the illustration.

8.2   ALOS2

The second dataset to be discussed is a dataset from the Advanced land observing satellite 2 (ALOS2), also with QUAD-POL mode. This data was collected from a region outside the north/west of Svalbard, on the third of April 2015. The time for the first and last zero doppler azimuth time was 21 : 25 : 53.584 and 21 : 27 : 03.58. Figure 8.4 shows the area where the ALSO2 data were collected.

The range sampling spacing was 2.86 m and the azimuth sample spacing was 2.78 m. The original raster height was 25960 lines and the original raster width was 8656 samples. To obtain a dataset not to large, the original dataset was decreased to raster height equal 10000 and raster width equal 4656. The antenna pointing direction was to the right.

People with vast experience within the filed advises that the data should be a composition of sea and different types of sea ice. Figure 8.5 shows the RGB colour composite using the multilooked radar cross section for the given scene.

This dataset does not have ground truth data consisting of ice thickness. However, it exists a Landsat8 dataset which covers the same scene as the ALOS2. The Landsat8 data was acquired on the same day as the ALSO2 data, only it was acquired six hours earlier. This corresponding Landsat8 data can be used to make an optical RGB image of the scene, which can be used to give an approximate classification, for example to the endmembers. The use of optical images as ground truth for SAR data has large limitations since it is only capable to separate a small number of different types of sea ice. Also, since there is some difference in time for when the two datasets were acquired, there can be changes in the scenery due to sea ice drift. Figur 8.6 shows the optical RGB image from the Landsat8 of the corresponding scene.
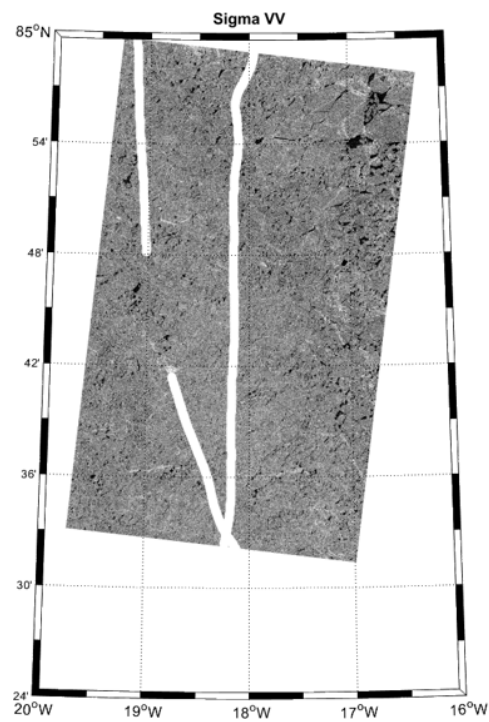
(a)   (b)

Figure 8.4: Image shows the area where the ALOS2 data was collected. This data was collected from a region outside the north/west of Svalbard. The image is produced using the program SNAP
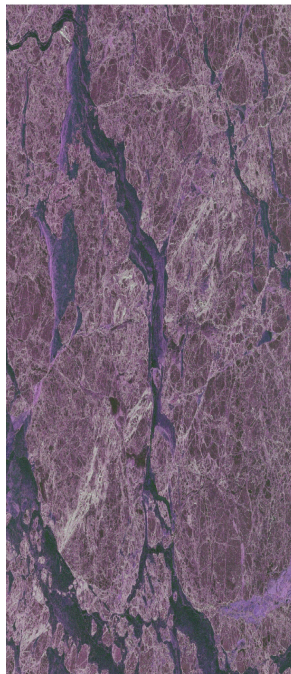
Figure 8.5: RGB colour composite using the multilooked radar cross section
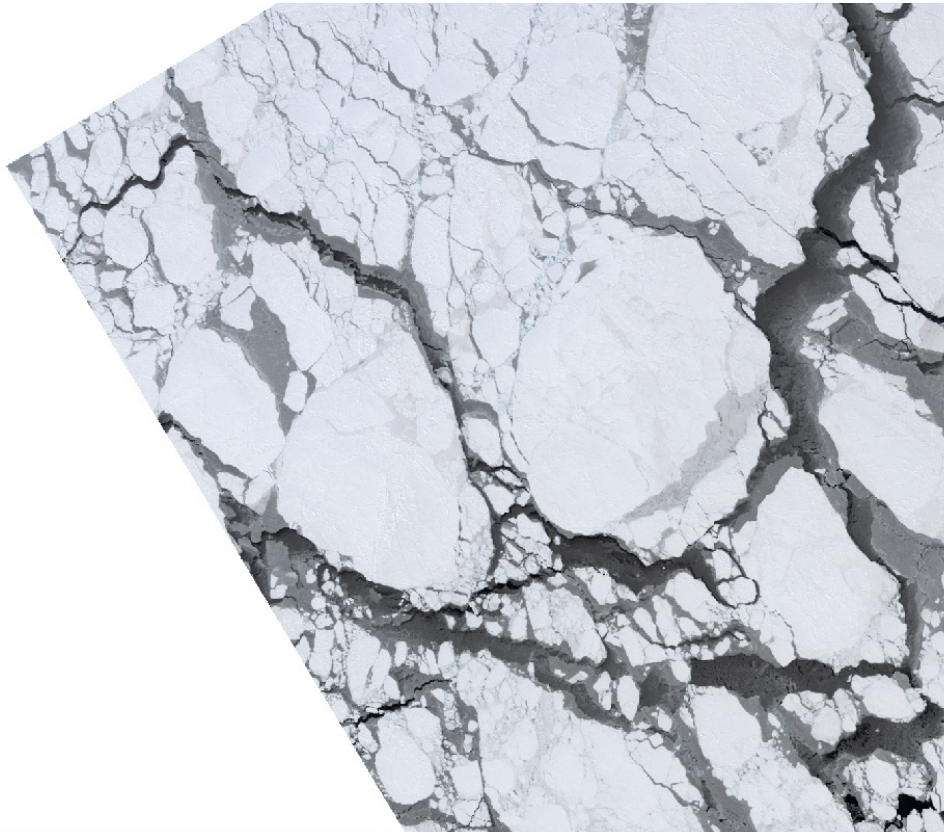
Figure 8.6: RGB optical image of the Landsat 8 data which have corresponding scene with the ALOS2 data. Image produced by Malin Johansson, Associate Postdoc, UiT. Got permission from her to use the illustration.

8.3 IceSAR

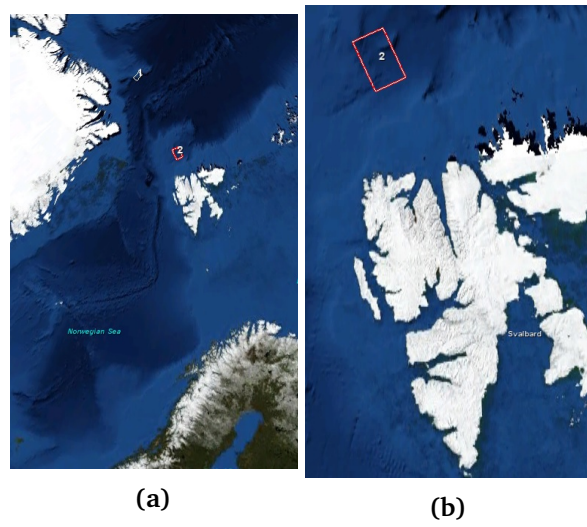The last dataset is not acquired from a satellite, but from a DLR airplane. The airplane had an altitude of 3000 m when acquiring the radar (ESAR) data. The data was acquired in March 2007. Optical data for the corresponding scene was acquired from an AWI airplane. The data is from a scene over drifting sea ice in Fram Strait. Both DUAL-POL and QUAD-POL modes were available in the dataset, but only the QUAD-POL data have been used in this project. The swath width was three km, incidence angle range 26-55 degree and the pixel size of 1.5 m. Figure 8.7a and 8.7b show the optical and the RGB colour composite image using the multilooked radar cross section of the scene.

The dataset did not have a ground truth consisting of ice thickness. In fact are we using the classification results from an another method, which we know have

achieved good results. The method is a region of interest (ROI) separability method, and is performed by the doctoral research student Johannes Philipp Lohse and Dr. Wolfgang Dierking, which both works at Centre for Integrated Remote Sensing and Forecasting for Arctic Operations (CIRFA). Figure 8.7c shows the classification results using the ROI separability. The bellow table (table 8.1) shows what type of class the different colors in figure 8.7c are representing.

Class 1	Open Water	dark blue
Class 2	Grey-white ice	light green
Class 3	Level ice	black
Class 4	Deformed ice	red
Class 5	Nilas	cyan
Class 6	Grey Ice	dark green

Table 8.1: The table lists the different classes in the IceSAR data and their corresponding color in the classification image 8.7c
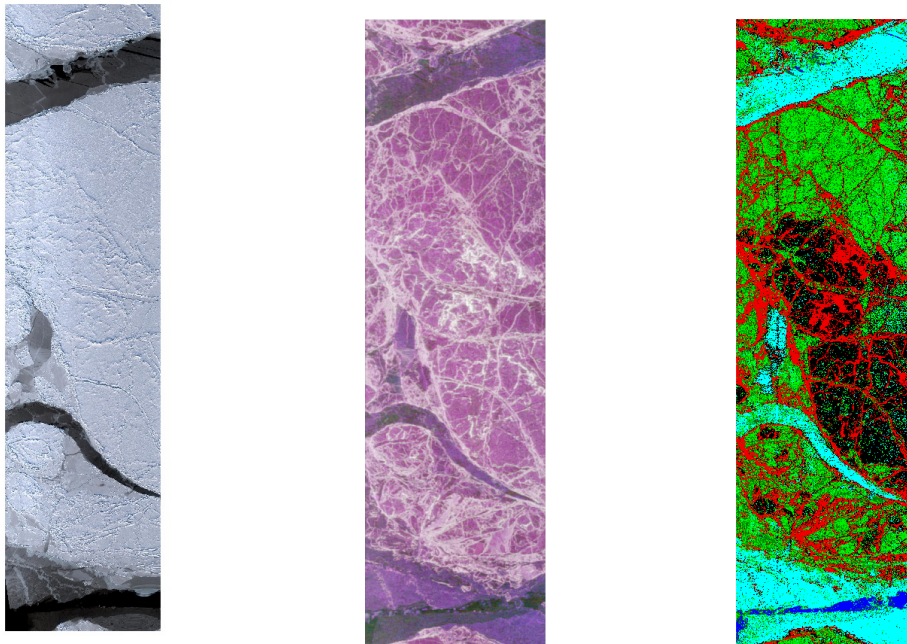
(a) RGB optical image of the Landsat8 data which have corresponding scene with the IceSAR data.

(b) RGB colour composite using the multilooked radar cross section

(c) The classification of the Ice-SAR data using the ROI separability method

Figure 8.7

/9

Computer Simulations and Experiments

The following chapter will cover and explain the computer simulations and experiments conducted on all the three datasets in order to evaluate the performance for the approach this thesis present. The different sections in this chapter will present how the different methods and algorithms, explained in the previous chapters, have been tested on the different datasets. The chapter is divided into three sections. First section describes the generation of the multidimensional feature space. This section also includes a description of the generation of synthetic data. The second section is related to the setup of the different algorithms and the third section is related to performance assessment.

9.1 Real and synthetic data

9.1.1 Real data

For all three QUAD-POL datasets, the same number and the same types of polarimetric features has been extracted. The extraction of the polarimetric features are based on the covariance matrix. The polarimetric features used to produce the datacubes for the different datasets was:

- The diagonal elements of the covariance matrix: $\mathbf{C}_{11}, \mathbf{C}_{22}, \mathbf{C}_{33}$

- The determinant of the sample covariance matrix: $det(\mathbf{C})$

- The three eigenvalues of the sample covariance matrix: $\lambda_1, \lambda_2, \lambda_3$

- The polarization fraction: PF

- The pedestal height: PH

Each multidimensional feature space datacube will therefore consist in a total of nine layers of polarimetric features, stacked upon each other.

9.1.2 Synthetic data

Generation of the synthetic data was conducted in order to provide more validation to the approach in this thesis. The endmembers extracted from the multidimensional feature space data belonging to the Radarsat2, the IceSAR and the ALOS2 data was used to make the synthetic data. The synthetic data is generated using the same rules and the same equation as for a linear mixing model.

$$\mathbf{y}_p = \sum_{r=1}^{R} \alpha_{r,p} \mathbf{m}_r + \mathbf{n}_p \tag{9.1}$$

Since the endmembers extracted from the Radarsat2, the IceSAR and the ALOS2 datacubes was used, the only missing parts was the abundance coefficients and the noise. The abundance coefficients were created by generating random numbers. The only two constrains for these numbers was that they could not be negative, and they had to sum to one for each sample. The missing noise was fixed by adding Gaussian noise. Figure 9.1 to figure 9.3 shows the signal to noise (SNR) for the synthetic datasets.
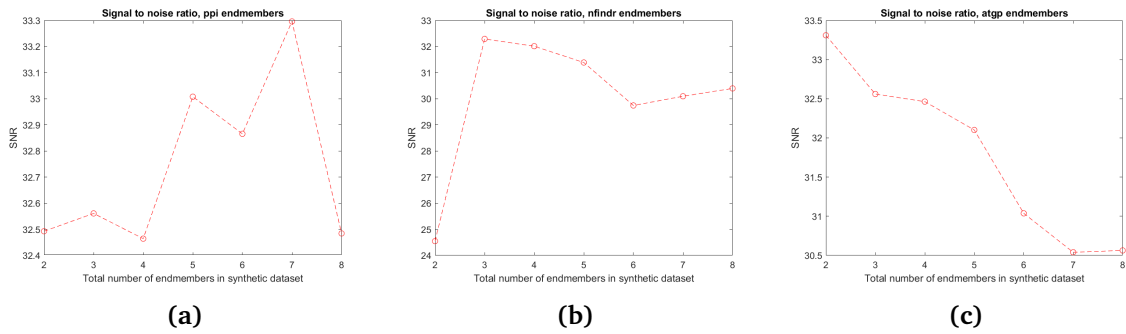
Figure 9.1: SNR for the synthetic data generated by using endmembers extracted from the Radarsat2 data. Figure (a) used the endmembers from PPI, figure (b) used the endmembers from NFINDR and figure (c) used the endmembers from ATGP.
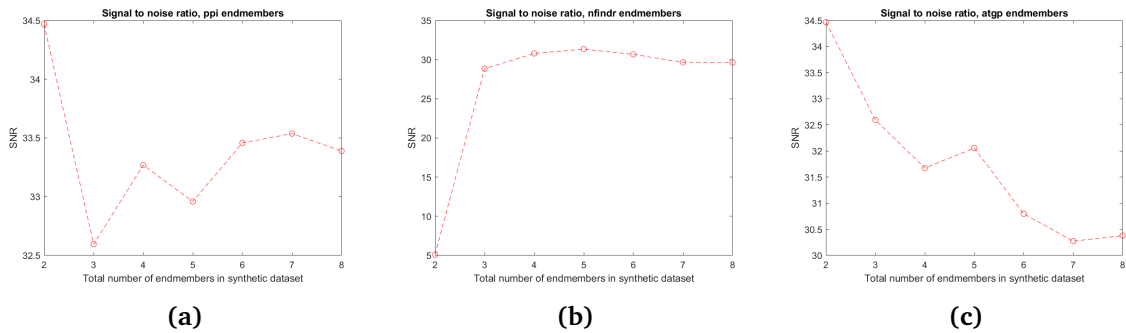
Figure 9.2: SNR for the synthetic data generated by using endmembers extracted from the ALOS2 data. Figure (a) used the endmembers from PPI, figure (b) used the endmembers from NFINDR and figure (c) used the endmembers from ATGP.
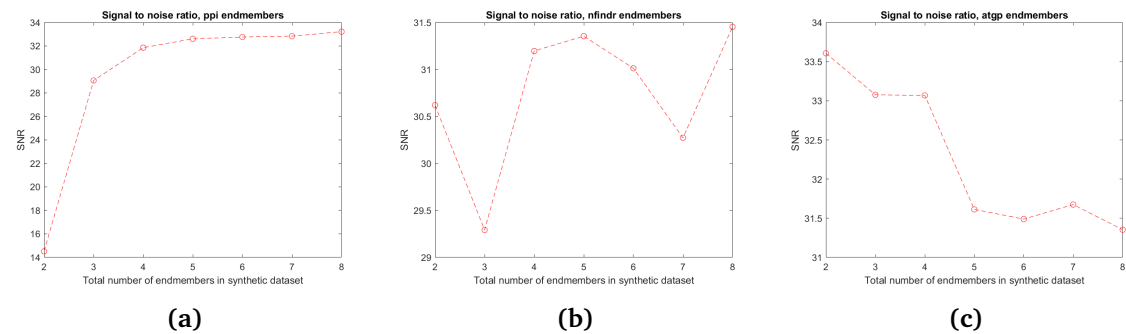
Figure 9.3: SNR for the synthetic data generated by using endmembers extracted from the IceSAR data. Figure (a) used the endmembers from PPI, figure (b) used the endmembers from NFINDR and figure (c) used the endmembers from ATGP.

9.2   The setup of the algorithms

9.2.1   Endmember extraction

The endmembers was extracted for all the datacubes, including the synthetic data. For this was the PPI, the NFINDR and the ATGP utilized. To compute the PPI algorithm, a function in the Hyperspectral Toolbox was used, which is a Matlab toolbox. This function is called hyperPpi. Further, 1000 skewers were used in the calculation. To compute the ATGP algorithm, the hyperAtgp function was used. This function is also from the Hyperspectral Toolbox. Needed to use another toolbox for computing the NFINDR. Used the EIA Toolbox and the function EIA-NFINDR to compute the NFINDR endmembers. Each algorithm has been used to extract several endmembers from two to eight.

### 9.2.2   OEN method

After extracting different number of endmembers, the OEN method was applied in order to calculate the number of classes in the scene. The OEN method was conducted on all the datasets, including the synthetic datasets.

9.2.3   FCLS

When the endmembers have been extracted and the number of classes in the scene has been calculated, the FCLS can be used to estimate the abundance fraction on the endmembers contribution to a target pixel feature. It was then assumed that the pixels were linearly mixed. For this project, the FCLS method has been used on all the datacubes. The FCLS method was also conducted on the synthetic data. These estimated abundance coefficients are, together with the endmembers, used to reconstruct the data. The goal is that the FCLS method will return good unmixing results when using the suggested number of endmembers, but the FCLS method were also applied using different numbers of endmembers. All of this is done in a linear manner.

Unmixing and reconstruction has also been done in a nonlinear manner by using the bilinear model (equation 3.3) and the constrains for a nonlinear mixing model(equation 3.4). The FCLS method was again used in order to estimate the abundance coefficients, but this time for both the linear abundance coefficients (α) and the nonlinear abundance coefficient(β). The input to the

FCLS method was therefore not only the linear form of the endmembers,

$$\mathbf{M} = [\mathbf{m}_1, \mathbf{m}_2, ..., \mathbf{m}_R] \tag{9.2}$$

but also the nonlinear

$$\mathbf{M}^k = [\mathbf{m}_1, \mathbf{m}_2, ..., \mathbf{m}_R]^k \tag{9.3}$$

where k is a number between two and P. As the FCLS method has large time complexity when using a large number of endmembers and the time left on the thesis was limited, the number of experiments using the nonlinear mixing model was limited. The nonlinear unmxing was only conducted on the IceSAR data using the endmembers extracted by the ATGP algorithm.

9.3   Performance assessment

9.3.1   Classification of the extracted endmembers

In order to validate the performance of the endmember extraction algorithms, we have utilized the different ground truths.

For the ground truth corresponding to the Radarsat-2 dataset, only a small part of the QUAD-POL data was represented with ground truth. In order to find the corresponding pixels, the corresponding coordinates (latitude and longitude) in the QUAD-POL data and the ground truth data had to be located. When knowing which samples in the Radarsat2 data which corresponds to the ground truth, the endmember extraction algorithms was conducted on these samples. By keeping track on the indexes of the samples which was characterised as pure pixels, the validation of the endmember extraction algorithms was done by checking if the algorithms were able to locate endmembers with different ice thickness.

The ALOS2 dataset did not have a ground truth consisting of ice thickens. It only had a corresponding optical image from the Landsat8 satellite. In order to validate the performance of the endmember extraction algorithms, the index for those samples which had been characterised as pure, needed to be hold on to. By marking the position of the pure pixels on for example an intensity image of the ALOS2 data, the corresponding position could be located in the optical image. Classification of the pure pixels was then done by looking on
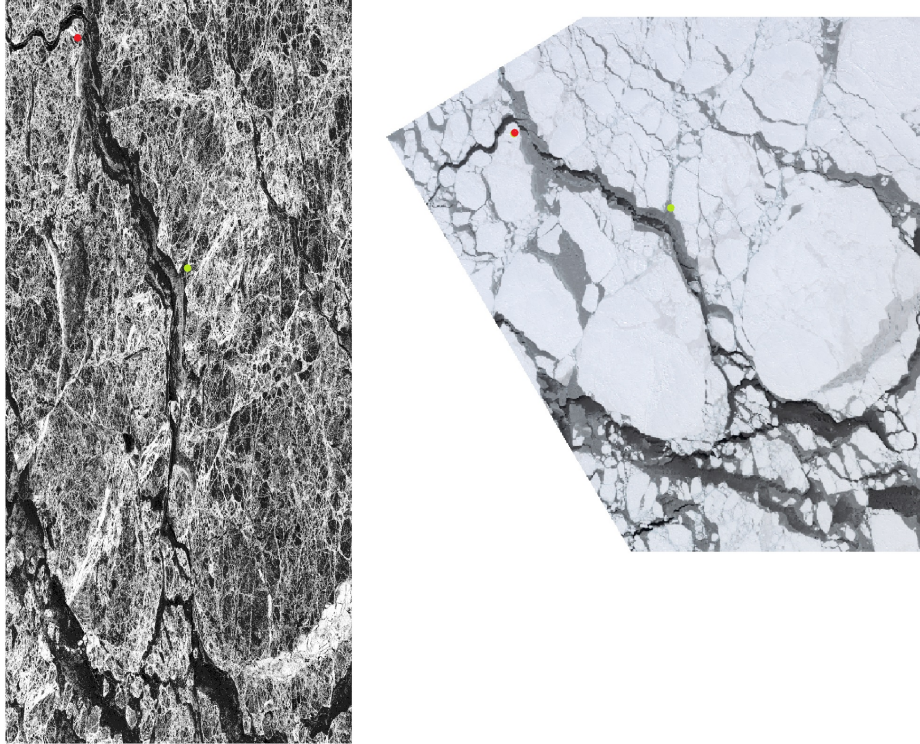
Figure 9.4: Two endmembers have been extracted using the ATGP algorithm on the ALOS2 data. Comparing the position of the endmembers in VV polarized intensity image with the optical image from Landsat8. The red dot is the first endmember and the green dot is the second endmember

the optical image to find what type of class the pure pixels represented. Again, this type of ground truth gives an extremely limited validation but can still provide an indication on the endmember extraction algorithms success on finding different types of pure pixels. Figure 9.4 shows an example on how the classification is done.

The last type of ground truth is the classification results using the ROI separability method. This ground truth corresponds to all the samples in the IceSAR data. In order to classify the extracted endmembers, the index of the samples that have been characterised as pure needed to be hold on to. Then, by comparing what the corresponding sample in the ground truth was classified as, the endmembers could be classified.

9.3.2   Validation of the OEN method

To validate the OEN method, the ground truth data belonging to the IceSAR data have been used. Further, by using the OEN method on the synthetic datasets, we can get a validation of the OEN method from these datasets as well. The validation is given because we always know how many classes each synthetic dataset consists of.

9.3.3   ARE

In order to get a validation on the performance of the reconstruction of the data and the FCLS, the ARE method is used. By using this method, it was possible to investigate how the different number of endmembers and the different endmembers extraction algorithm affected the unmixing results. The ARE was calculated for all the reconstructed data.

9.3.4   Classification

Classification of all the pixels in a scene can be done when the endmembers abundance fraction contribution to a pixel has been finalized. By finding the endmember with the largest fractional contribution on a pixel, the given pixel can be classified as the same class which the endmember is. In this project have classification of every pixel been done for the IceSAR dataset, both using the linear and nonlinear mixing model.

9.3.5   Average abundance error

To calculate the ability for the FCLS to estimate the abundances coefficients, we use the AAE by comparing the estimated abundances coefficients with the original abundances coefficients. The calculation of the AAE were only done for the synthetic datasets because these were the only datasets where the original abundance was known.

10

Results and Discussion

We shall now continue to discuss the most important and interesting results for all the experimental testes and simulations explained in the previous chapter. This is in order to validate if the approach in this thesis works or not.

10.1 Endmember extraction algorithms

In this section we will cover and discus the results of using the different endmember extraction algorithms on the Radarsat2, the ALOS2 and the IceSAR dataset.

10.1.1 Radarsat2 data

In order to validate the performance of the endmember extraction algorithms on the Radarsat2 scene, the algorithms were tested on the ground truth. Table 10.1 to table 10.3 shows the ice thickness of the endmembers using the extraction algorithms on the ground truth data. The tables shows the results of using two to four endmembers.

The results from the ground truth dataset is quite poor as the extracted endmembers had very similar ice thickness. Most of the endmembers were classified as ice with thickness between 0.8 meters to 2.2 meters. Figure 10.1 shows the

distribution of the ice thickness for the samples in the ground truth dataset. It also shows that there exists ice in the scene that are thicker then teen meters. Good results from the extraction algorithms would resulted in endmembers with a larger difference in the ice thickness.

The bad results have probably been caused by the distribution of the data regarding the ice thickness. The ice thickness was gamma distributed. The samples which are lager then 3 meters, are few compared to those between 0.8 and 2.4 meter. Accordingly, these few samples becomes outliers and are located far away from the data manifold. The three endmember extraction algorithms will therefore have trouble locating all the pure pixels in the data. If the distribution of the ice thickness was more uniform, the results would probably have been better.

Endmember nr.	Ice thickness
1	2.1930
2	1.4920

Endmember nr.	Ice thickness
1	2.1930
2	1.0400
3	0.6750

Endmember nr.	Ice thickness
1	2.1930
2	1.0400
3	0.6750
4	1.4920

Table 10.1: Endmember classification. The table shows the ice thickness for the different endmembers extracted using PPI

Endmember nr.	Ice thickness
1	2.1930
2	1.4920

Endmember nr.	Ice thickness
1	1.4920
2	2.1930
3	0.8150

Endmember nr.	Ice thickness
1	1.0400
2	2.2940
3	2.1930
4	0.6750

Table 10.2: Endmember classification. The table shows the ice thickness for the different endmembers extracted using NFINDR

Endmember nr.	Ice thickness
1	1.4920
2	0.5270

Endmember nr.	Ice thickness
1	1.4920
2	0.5270
3	2.1930

Endmember nr.	Ice thickness
1	1.4920
2	0.5270
3	2.1930
4	0.6750

Table 10.3: Endmember classification. The table shows the ice thickness for the different endmembers extracted using ATGP
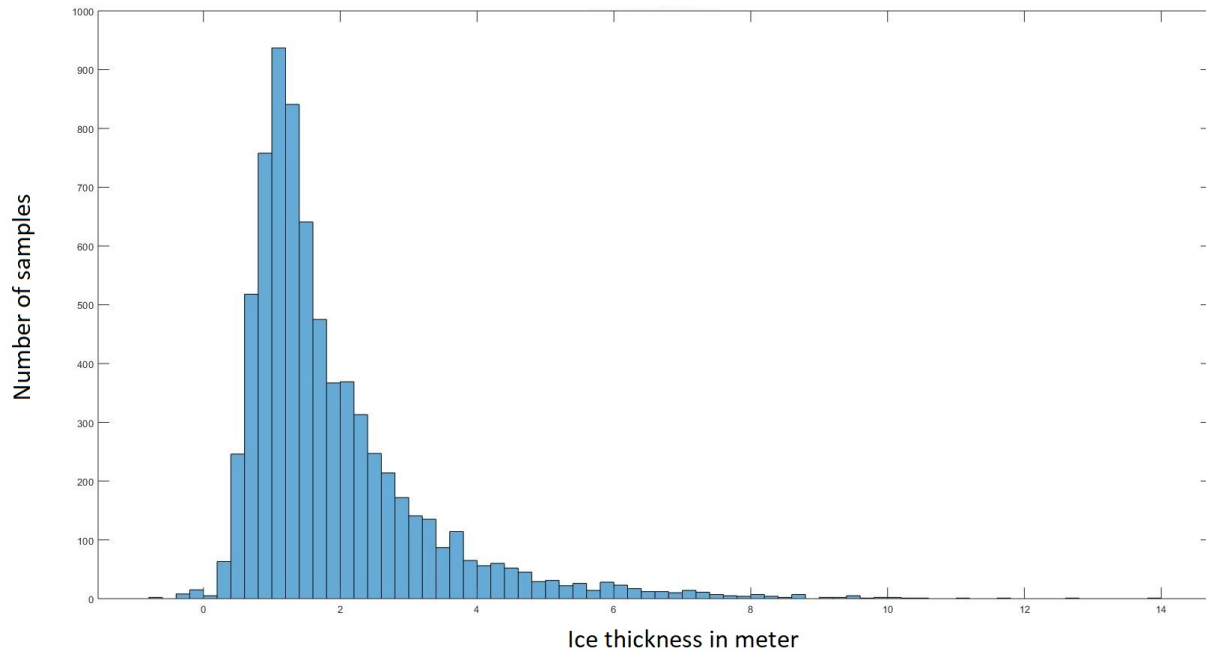
Figure 10.1: The distribution of the ice thickness in the ground truth dataset, x-axis is the ice thickness in meters and axis is the number of sample.

10.1.2 ALOS2

Figure 10.3, figure 10.5 and figure 10.7 shows the position of the extracted endmembers on the intensity image of the scene using the VV polarization. The endmembers are extracted from the ALOS2 data using the different endmember extraction algorithms. The figures shows the results of using two to four endmembers. One will note from the figures that the endmembers are well separated from each other. These results are possible to use in order to obtain a validation on the performance of the endmember extraction algorithms.

To receive the required validation discussed above, the corresponding Landsat8 data was used. Figure 10.4, figure 10.6 and figure 10.8 shows where the endmembers are located in the Landsat8 scene

By looking at figure 10.4 (a), figure 10.6 (a) and figure 10.8 (a), it is possible to note that all the endmember extraction algorithms detected different types of classes for all the three endmembers. All the algorithms had one endmember for open water, one endmember for thicker ice and one endmember for thinner ice.

In regards to figure 10.4 (b), figure 10.6 (b) and figure 10.8 (b), which shows the results using four endmembers, it is difficult to see what the fourth end-member is. The fourth endmember for PPI appears as thicker ice, like the first PPI endmember. The situation is similar for the fourth endmember for both the NFINDR and ATGP algorithm. For the NFINDR algorithm, the fourth extracted endmember appears as thin ice, similar as the first endmember. The fourth extracted endmember using ATGP appears as thicker ice, like the first endmember. At this number of endmembers, this type of ground truth is limited in order to classifying the endmembers. Still, the ground truth indicates that the endmember extraction algorithms had success in finding different types of pure pixels.

However, even though the ground truth can't tell if the four extracted endmembers are different from each other, it is still possible to answer the question. By calculating the Euclidean distance between the four extracted endmembers, it is possible to verify if the endmembers are different from each other. Table 10.4, 10.5 and 10.6 shows the results of calculating the Euclidean distance between the four extracted endmemers. The table 10.5 and 10.6 tells us that the four endmembers extracted using the NFINDR and ATGP algorithm are not similar, because the values in the tables are big and not small. However, the fourth endmember extracted by the PPI algorithm is similar to the first endmember, because the value is small. The smaller the values are, the more similar are the endmembers. Accordingly, when the value is zero the endmembers will be identical. One can also see this by studding figure 10.2, where endmember one and four have similar polarimetric values, resulting in similar shape on the plot.

	Endmember 1	Endmember 2	Endmember 3	Endmember 4
Endmember 1	0	2.1552	2.2410	0.9108
Endmember 2	2.1552	0	2.2325	2.1138
Endmember 3	2.2410	2.2325	0	1.6761
Endmember 4	0.9108	2.1138	1.6761	0

Table 10.4: The table shows the Euclidean distance between the four endmemers extracted using the PPI algorithm

	Endmember 1	Endmember 2	Endmember 3	Endmember 4
Endmember 1	0	2.2325	2.2410	1.6706
Endmember 2	2.2325	0	2.1552	1.3584
Endmember 3	2.2410	2.1552	0	2.0203
Endmember 4	1.6706	1.3584	2.0203	0

**Table 10.5:** The table shows the Euclidean distance between the four endmemers extracted using the NFINDR algorithm

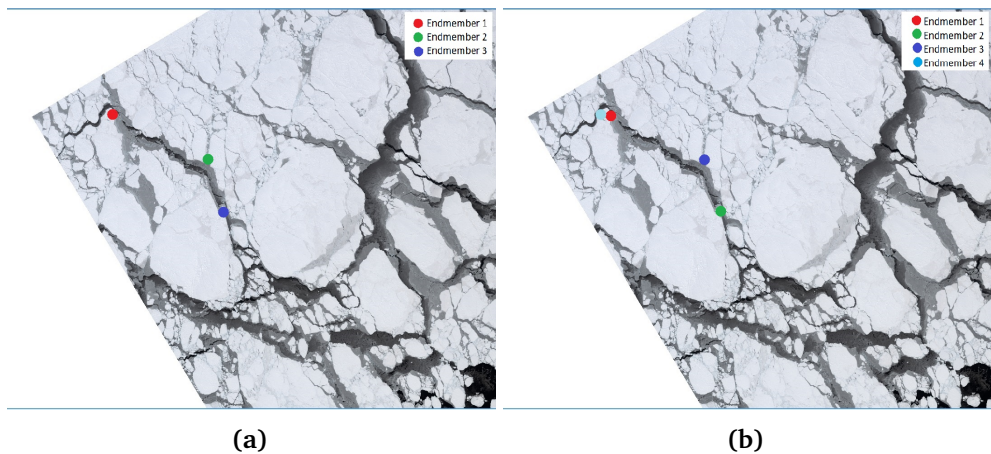|	Endmember 1	Endmember 2	Endmember 3	Endmember 4
Endmember 1	0	2.4110	2.1552	1.5375
Endmember 2	2.2410	0	2.2325	1.7401
Endmember 3	2.1552	2.2325	0	1.5191
Endmember 4	1.5375	1.74401	1.15191	0

Table 10.6: The table shows the Euclidean distance between the four endmemers extracted using the ATGP algorithm
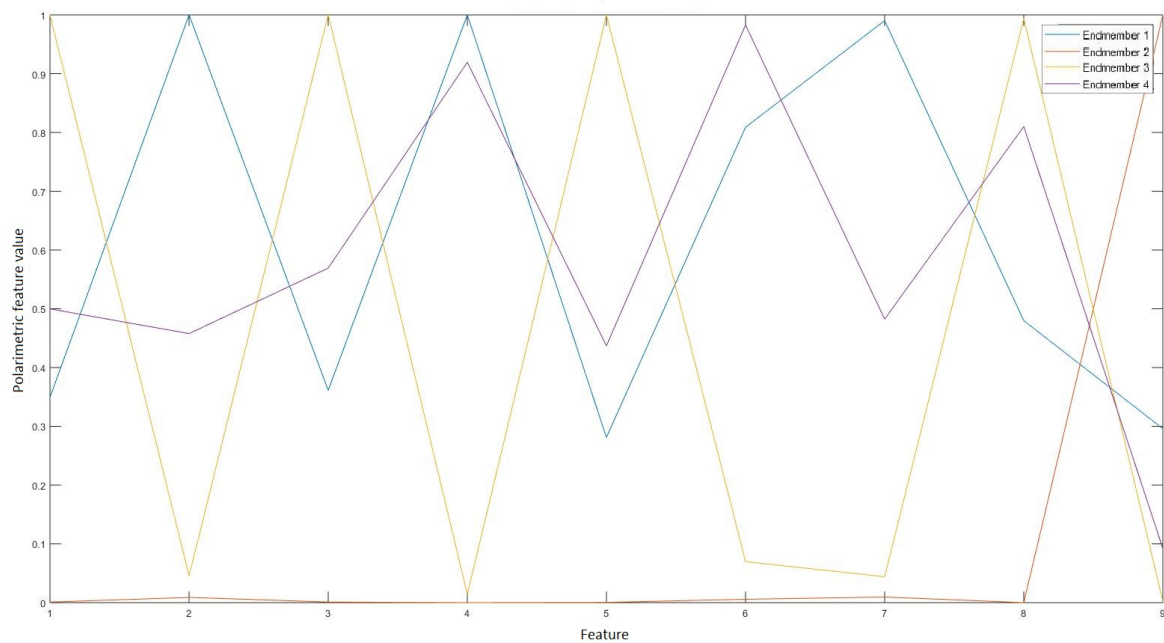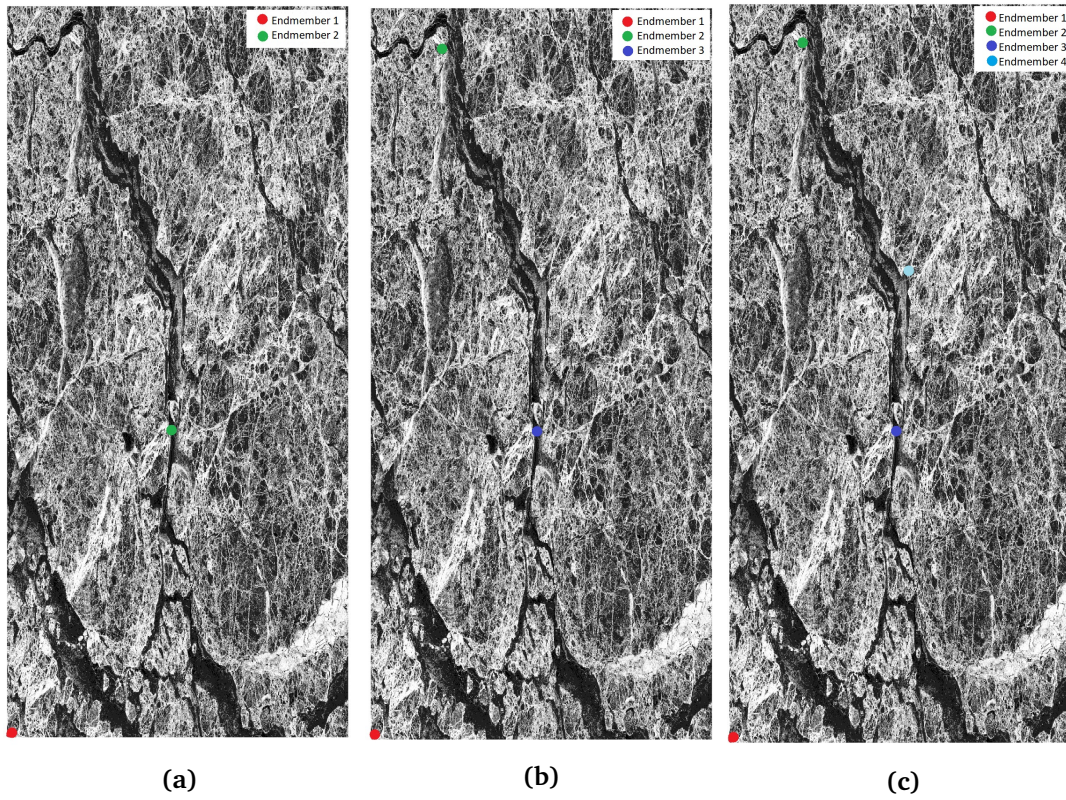

Figure 10.2: The polarimetric values for the four endmembers extracted by PPI

(a)   **(b)**   **(c)**
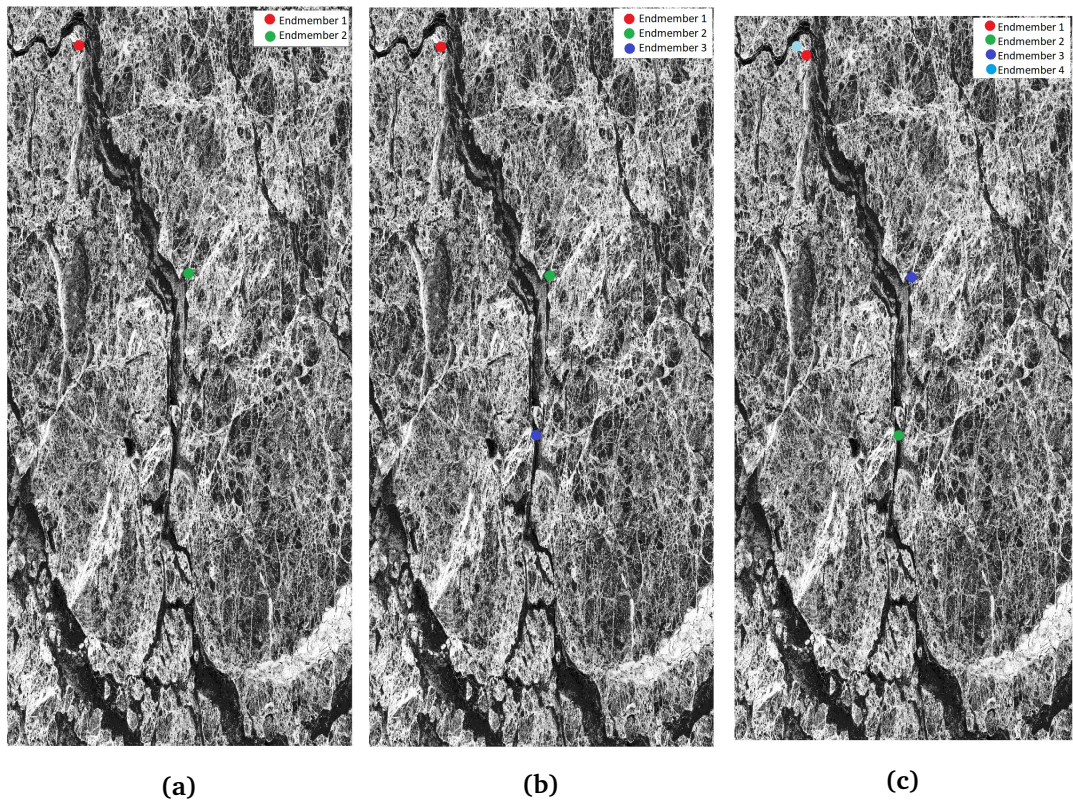
Figure 10.3: The position in the VV intensity image for the two to four endmembers extracted using PPI algorithm. Figure (a) shows two extracted endmembers. Figure (b) shows three extracted endmembers. Figure (c) four extracted endmembers.

(a)   **(b)**

Figure 10.4: The corresponding position for the PPI endmembers in RGB image from the Landsat8 data. Figure (a) shows three extracted endmembers and figure (b) shows four extracted endmembers.

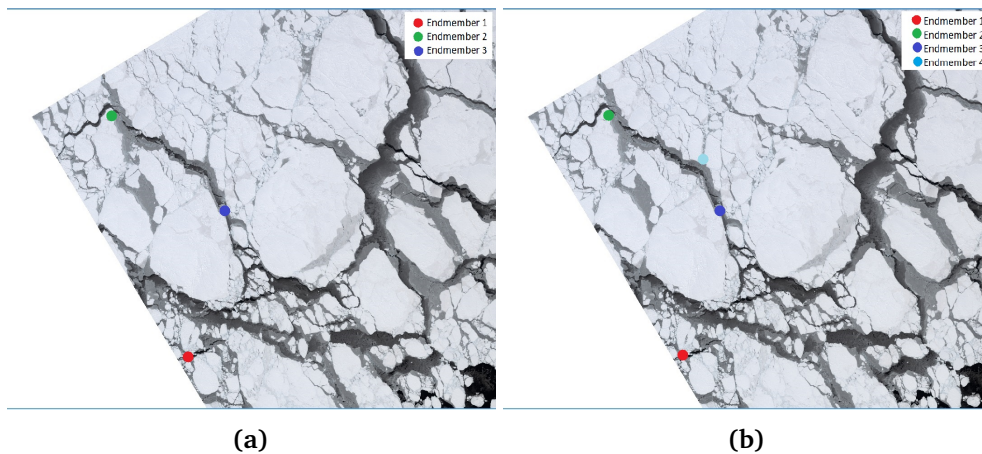(a)   (b)   (c)

Figure 10.5: The position in the VV intensity image for the two to four endmembers extracted using NFINDR algorithm. Figure (a) shows two extracted endmembers. Figure (b) shows three extracted endmembers. Figure (c) four extracted endmembers.

(a)   (b)

Figure 10.6: The corresponding position for the NFINDR endmembers in RGB image from the Landsat8 data. Figure (a) shows three extracted endmembers and figure (b) shows four extracted endmembers.

Figure 10.7: The position in the VV intensity image for the two to four endmembers extracted using ATGP algorithm. Figure (a) shows two extracted endmembers. Figure (b) shows three extracted endmembers. Figure (c) four extracted endmembers.
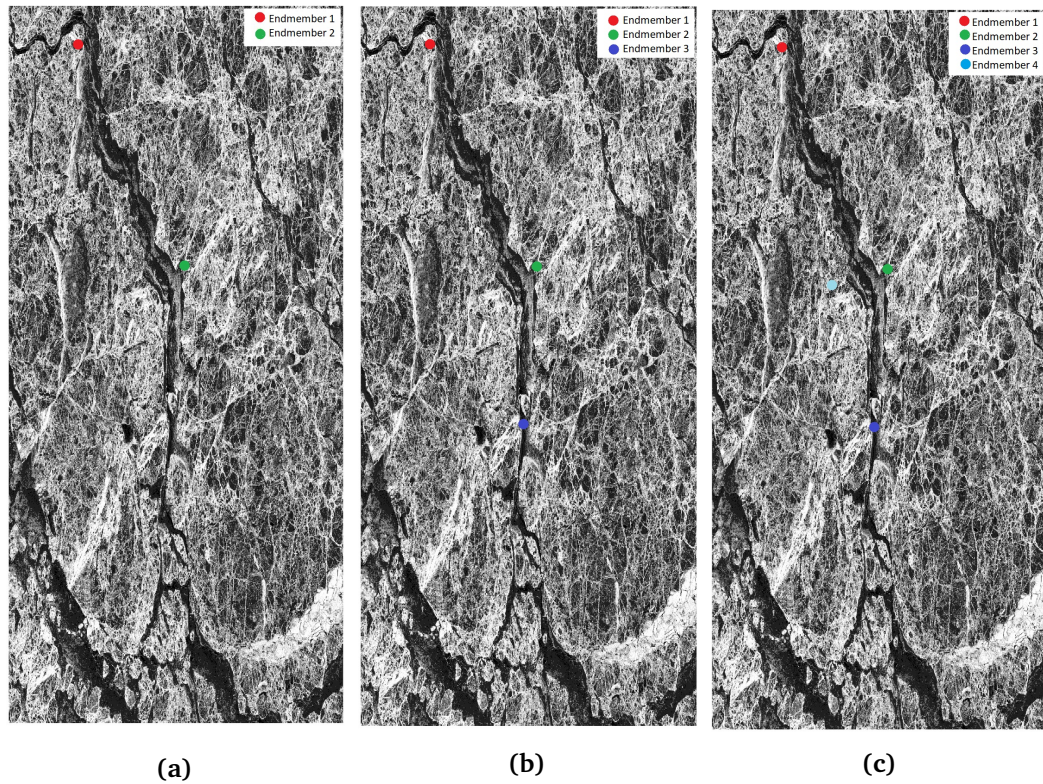

Figure 10.8: The corresponding position for the ATGP endmembers in RGB image from the Landsat8 data. Figure (a) shows three extracted endmembers and figure (b) shows four extracted endmembers.
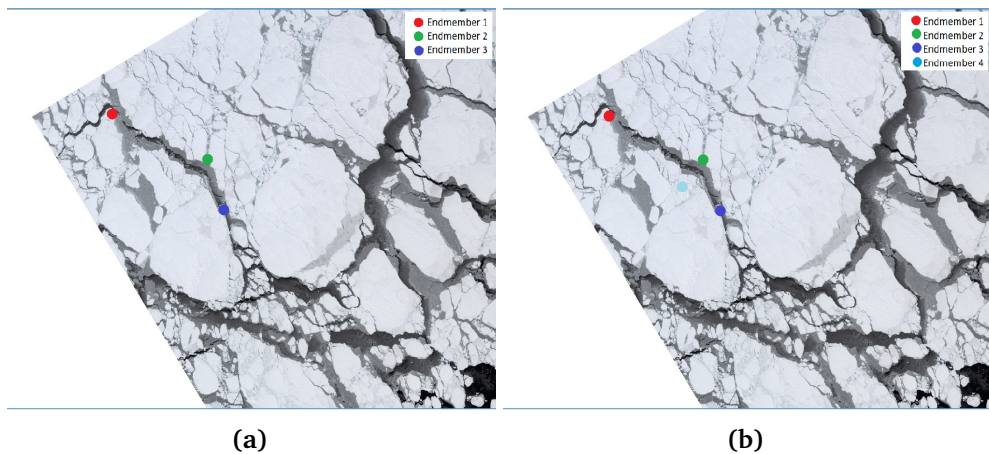
10.1.3   IceSAR data

The IceSAR dataset had a groundtruth which corresponded to all of the samples in the dataset. This makes it possible to classify every endmember extracted by the algorithms and give a proper verification on how good these endmember extraction algorithms are. In total, this ground truth consisted of six classes which was open water, grey-white ice, level ice, deformed ice, nilas and grey ice. Table 10.7 shows the result for the classification of the endmembers. The table covers the endmembers sets consisting of two to six endmembers. From these results was the PPI algorithm the worst algorithm, and it delivered really poor results. In total it only managed to extract three different endmember classes and the first two endmembers it extracted was both open water endmembers. The NFINDR algorithm gave us better results. It managed to extract five different endmember classes when the algorithm was set to find five endmembers, but it only located four different endmember classes when the algorithm was set to extract six endmembers. The best algorithm was the ATGP. It managed to extract all the 6 different endmember classes.

Overall, both the NFINDR and ATGP endmember extraction algorithm delivered good results, as they managed to find several different pure pixels, for both the ALOS2 and the IceSAR dataset. However, the results from the PPI algorithm was not equally good. For the approach to successfully manage to retrieve information from earth surface, good results when extracting the endmembers will be crucial. A potential reason for the poor results using the PPI algorithm could be that the number of skewers was too low. Attempts on increasing the number of skewers was made, but it resulted in high computational cost, especially on these large sea ice datasets.

Total number of endmembers	Endmember	PPI	NFINDR	ATGP
2	1st	Open water	Deformed ice	Deformed ice
	2nd	Open water	Open water	Grey ice
3	1st	Open water	Deformed ice	Deformed ice
	2nd	Open water	Open water	Grey ice
	3rd	Deformed ice	Nilas	Open water
4	1st	Open water	Level ice	Deformed ice
	2nd	Open water	Deformed ice	Grey ice
	3rd	Level ice	Open water	Open water
	4th	Deformed ice	Nilas	Grey-white ice
5	1st	Open Water	Level ice	Deformed ice
	2nd	Open Water	Deformed ice	Grey ice
	3rd	Deformed ice	Grey-white ice	Open water
	4th	Deformed ice	Open water	Grey-white ice
	5th	Level ice	Nilas	Nilas
6	1st	Open water	Level ice	Deformed ice
	2nd	Open water	Deformed ice	Grey ice
	3rd	Deformed ice	Deformed ice	Open water
	4th	Level ice	Grey-white ice	Grey-white ice
	5th	Deformed ice	Open water	Nilas
	6th	Deformed ice	Open water	Level ice

Table 10.7: The table shows classification results of the endmembers.

10.2   Optimal endmember number

To give a validation of whether or not the OEN method works, both real and synthetic dataset have been used. The most interesting results using the OEN method are illustrated and discussed in the following section.

10.2.1   ALOS2

For the ALOS2 dataset the OEN method suggested four endmembers for both the endmembers extracted by the NFINDR and the ATGP algorithm. It suggested three endmembers when using the endmembers extracted by the PPI algorithm. The result are shown in figure 10.9.

This dataset does not have a good enough ground truth to verify that the method suggested the correct number of endmembers/classes. From chapter 10.1.3, we know that the endmembers extracted using the PPI algorithm would, most likely, only be able to locate three different classes. Accordingly,
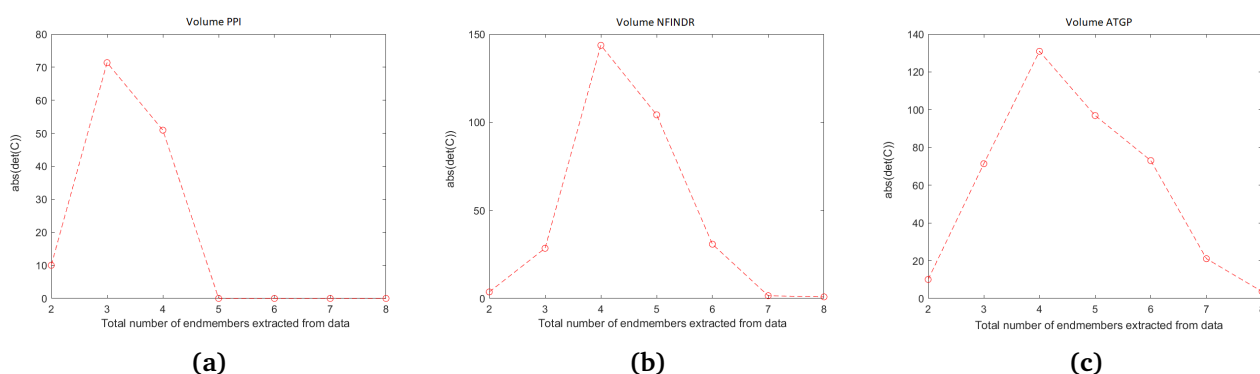
Figure 10.9: The results of the calculated volume using different number of endmembers extracted from the ALOS2 dataset. Figure (a) are the endmembers from the PPI algorithm, figure (b) is the endmembers from the NFINDR algorithm and figure (c) is the endmembers from the ATGP algorithm.

the OEN method suggested the correct number of classes. Regarding the endmembers extracted by using the NFINDR and the ATGP algorithm, is it likely that the number of classes are four, which is the number the OEN method suggested.

The reason why the suggested number of classes in the scene is so low is probably because the fifth and sixth extracted endmember are so similar compared to the other endmembers. The approach using the endmember extraction algorithm and the OEN method therefore don't categorize these endmembers as pure pixels.

10.2.2   IceSAR

The only dataset with a ground truth able to tell the number of classes in the scene is the IceSAR dataset. Still, as this ground truth is a result from another classification method is it no guaranty that six classes are the correct number. There is however a chance that there are more than six classes in the scene. It all depends on the sensitivity of the method in order to find different classes. In any case, ROI separability method is a good and trusted method for classification.

The results using the OEN method on the IceSAR scene gave the results shown in figure 10.10. The method suggested five classes for both the endmembers extracted by the ATGP and the NFINDR algorithm. It suggested four endmembers when using the endmembers extracted by the PPI algorithm. For the NFINDR endmembers, the OEN method suggested the same number of endmembers as the NFINDR algorithm located, hence it worked perfectly for this
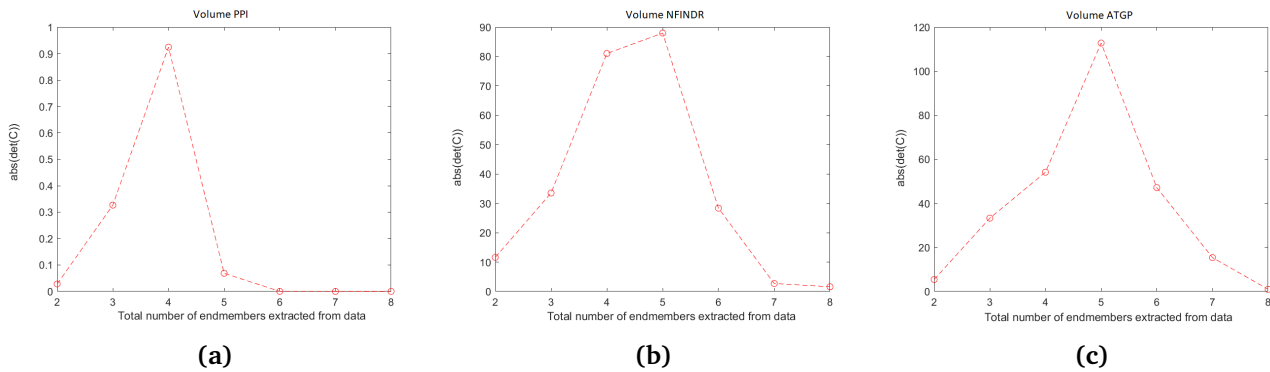
Figure 10.10: The result of the calculated volume using different number of endmembers extracted from the IceSAR dataset. Figure (a) are the endmembers from the PPI algorithm, figure (b) is the endmembers from the NFINDR algorithm and figure (c) is the endmembers from the ATGP algorithm.

set of endmembers. For the PPI and the ATGP endmembers, the method did not suggest the same number of endmembers as the algorithms were capable of extracting.

For the PPI endmembers, the method actually suggested four endmembers, which is one more then the PPI algorithm was capable of extracting. The bad result has been caused by the PPI algorithm, which stared with extracting two "similar" endmembers. Both of them was open water (table 10.7). As a result, the volume when using two similar endmembers became extremely low (figure 10.10 (a)). When three endmembers were extracted, the PPI algorithm had extracted two open water endmembers and one deformed ice endmember, resulting in an increase of volume. The same happened when four endmembers were extracted, because the PPI managed to extract two open water endmembers, one deformed ice endmember and one level ice endmember. When extracting 5 endmembers, the PPI algorithm still only managed to extract three different types of endmembers. The algorithm extracted two open water endmembers, two deformed ice endmembers and one level ice endmember. The result, a decrease in volume because the extracted endmembers was similar to each other.

The ATGP algorithm were capable of extracting six different endmembers, but the OEN method suggested only five. There could be many reasons for this. One reason could be that the shape and the distribution of the data manifold in the nine-dimensional space gives a larger volume when using five endmembers instead of six. Figure 10.11 shows an illustrative example, but in a two-dimensional space, on how the shape and distribution of the data manifold can provide a smaller volume/area when using the correct number of endmembers compared to using one less endmember.
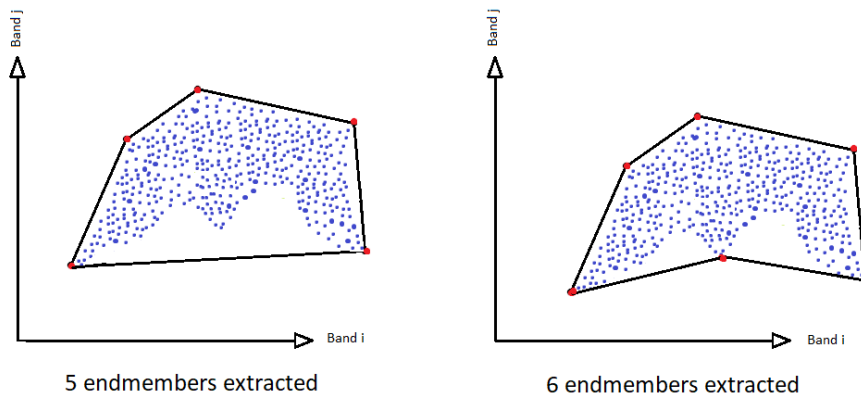
Figure 10.11: An example on how the area spanning the data manifold can decrease when using six endmembers instead of five. Using six endmembers would have represented the data better then only using five
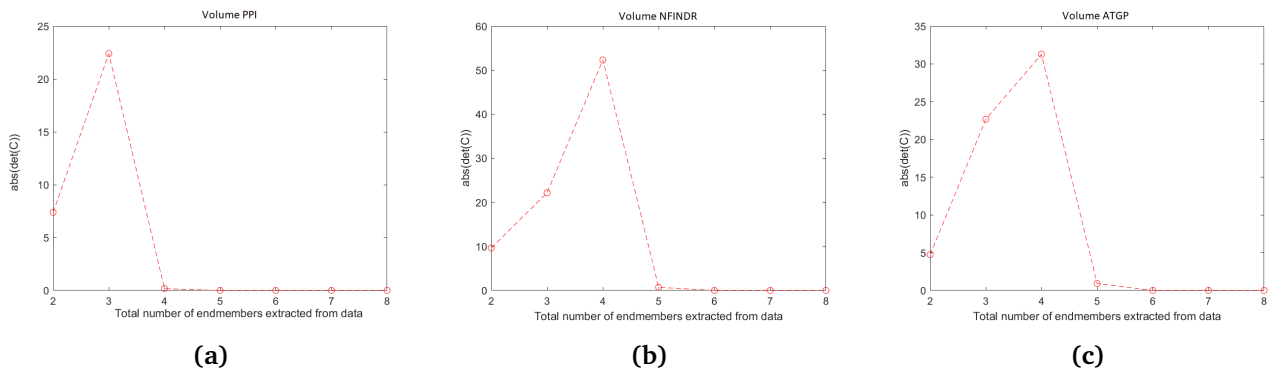
10.2.3 Synthetic data

In addition, synthetic datasets were generated by using the endmembers extracted from the IceSAR scene. For the synthetic dataset containing four classes, the results from the OEN method is shown in figure 10.12. When using the endmembers extracted by the ATGP and NFINDR algorithm, the OEN method suggested four endmembers. In other words, it suggested the correct number of classes. The results were not equally good when using the endmembers extracted by PPI. The method then suggested three endmembers. This is a result of the PPI algorithm delivering bad endmember extraction results. The PPI algorithm is not capable of locating four endmembers which are different compared to each other. Accordingly the OEN method will only suggest three classes.

Figure 10.13 shows the results from the OEN method used on the synthetic dataset containing five classes. It suggested three endmembers when using the endmembers extracted by the PPI algorithm. The result was much better when the method used the endmembers extracted by the NFINDR and ATGP algorithm. It then suggested five endmembers, which is the correct number of classes in the dataset. The NFINDR and the ATGP extraction algorithm are capable of locating five endmembers which are different compared to each other. Extracting six endmembers resulted in similar endmembers. The simplex volume using six endmembers was therefore lower than the simplex volume using five endmembers.

The results using the OEN method on the synthetic data was good, especially when the method used the endmembers extracted by the NFINDR and ATGP

algorithms. The reason for this is probably because the shape and distribution of the data manifold in the synthetic data are not affected with the same challenges as the sea ice data can suffer for. Figure 10.14 shows a three-dimensional scatteringplot of the samples in the synthetic dataset generated using four endmembers from the IceSAR data. The data manifold with these three features will not be affected by the earlier mentioned challenge.

(a)   (b)   (c)

Figure 10.12: The result of the calculated volume using different number of endmembers extracted from from synthetic data containing four classes. Figure (a) are the endmembers from the PPI algorithm, figure (b) is the endmembers from the NFINDR algorithm and figure (c) is the endmembers from the ATGP algorithm.

(a)   (b)
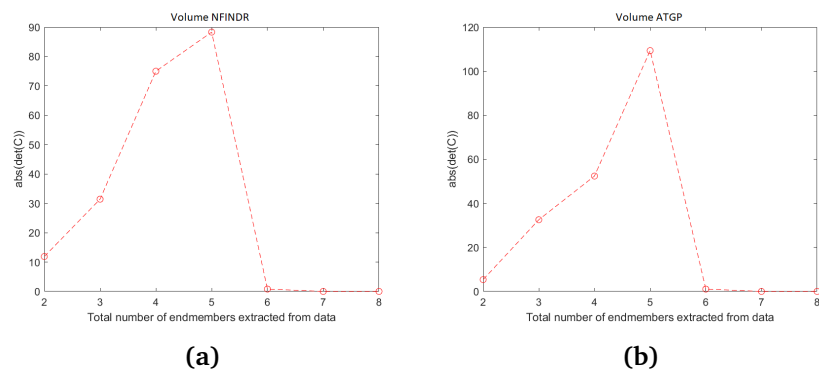
Figure 10.13: The result of the calculated volume using different number of endmembers extracted from synthetic data containing five classes. Figure (a) are the endmembers from the NFINDR algorithm and figure (b) is the endmembers from the ATGP algorithm
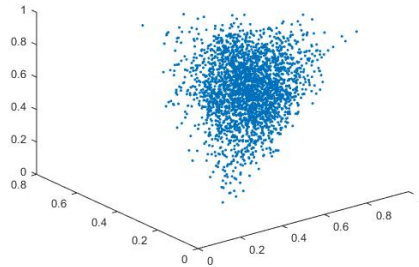
(a)

Figure 10.14: The figure shows a three-dimensional plot of the samples in the synthetic
dataset generated using four endmembers from the IceSAR data.

10.3 Unmixing

To unmix the mixed pixels, the FCLS method have been used, the method
estimates the abundance coefficients. To validate the performance of the FCLS,
several alternatives has been considered and tested. The most interesting
results are illustrated and discussed in this section.

10.3.1 ARE

The linear mixing model is used to achieve all the results presented in this
subsection.

We shall start at the ARE results from the Radarsat2 data, figure 10.15. The
ARE resulted in high values when the number of endmembers, extracted by
the NFINDR and ATGP, were low. However, the error value rapidly decreased
when the number of endmembers became larger. The ARE value, using the
endmebers extracted by ATGP, decreased on the sixth endmember. The ARE
value, using NFINDR endmembers, decreased on the fifth endmember. Fig-
ure 10.16 and figure 10.17 shows how the pixel reconstruction error changes
during this rapid decrease in ARE. The pixel reconstruction error shows the
reconstruction error in every pixel for the reconstructed data. Can see from
the figures how the error in each pixel is highly reduced.

Concerning the ARE result using the endmembers extracted by the PPI algo-
rithm (figure 10.15 a), the result did not have the same behaviour as results
using the ATGP and NFINDR endmembers. The error does not decrease

sharply as it does using the NFINDR and the ATGP endmembers. When using two endmembers the ARE value is 0.5 and when using four endmembers the ARE value have decreased to approximately 0.25. Adding more endmembers gave minimal decrease in the ARE value. This result is probably due to the bad results coming from the PPI endmember extraction algorithm.

The ARE results for the ALOS2 and the IceSAR dataset was similar to the results using the Radarsat2 data. Figure 10.18 shows the ARE results for the IceSAR data. The next sub section will contain a discussion on potential causes for the results.

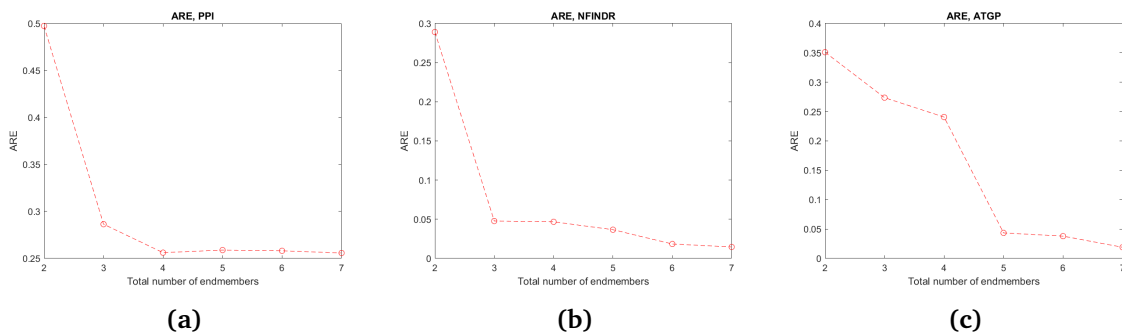**(a)**   **(b)**   **(c)**
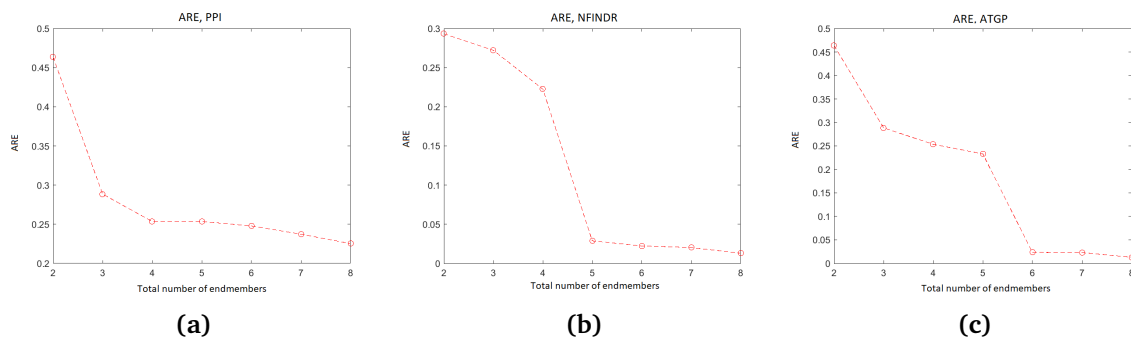
Figure 10.15: The ARE results on the Radarsat2 dataset. In figure (a) are the endmembers from the PPI algorithm used, in figure (b) are the endmembers from the NFINDR algorithm used and in figure (c) are the endmembers from the ATGP algorithm used.

(a)   **(b)**
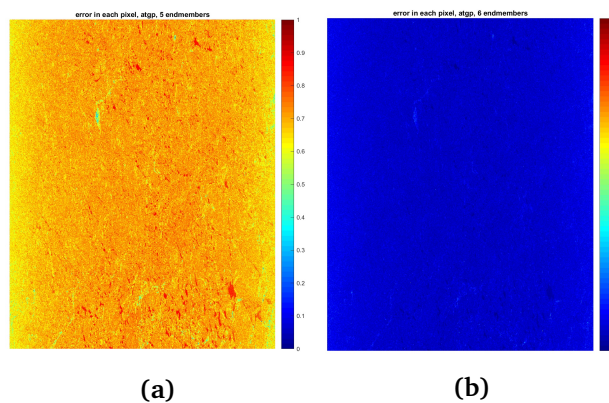
Figure 10.16: Pixel reconstruction error for reconstructed data using ATGP endmembers from the Radarsat2 data. Red colour indicates a large error whilst blue colour indicates a low error . Figure (a) have used five endmembers when reconstructing the data and figure (b) have used six endmembers when reconstructing the data.

(a)   (b)
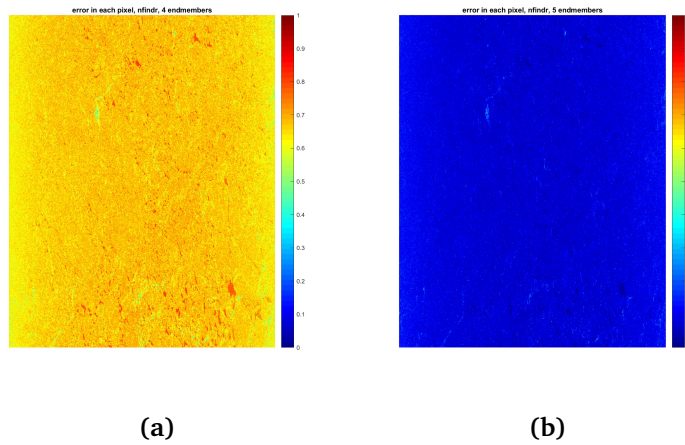
Figure 10.17: Pixel reconstruction error for reconstructed data using NFINDR end-
members from the Radarsat2 data. As in the above, red colour shows
large error whilst blue colour indicates low error. Figure (a) have used
five endmembers when reconstructing the data and figure (b) have used
six endmembers when reconstructing the data.

(a)   (b)   (c)

Figure 10.18: The ARE results on the IceSAR dataset. In figure (a) are the endmembers
from the PPI algorithm used, in figure (b) are the endmembers from
the NFINDR algorithm used and in figure (c) are the endmembers from
the ATGP algorithm used.

10.3.2   Abundance and classification using linear mixing model

In order to classify the samples in the data, we need to find the endmember
which has the largest fractional contribution on each sample. This can be
done by finding which endmember that has the largest abundance value for
each sample. The IceSAR dataset is the only dataset where it is possible to
validate the classification results. Figure 10.19 shows the classification of the
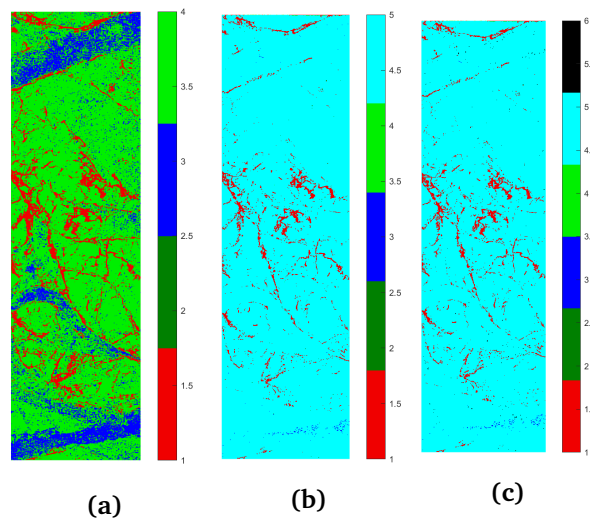
Figure 10.19: Classification of the samples using four (a) endmembers, (b) five end-
members and (c) six endmembers extracted by the ATGP algorithm.
Dark blue color is open water, light green is grey white ice, black is level
ice, red is deformed ice, cyan is nilas and dark green is grey ice.

samples using four to six endmembers. All the endmembers were extracted
by the ATGP algorithm. The resulting classification was poor. The correct
classification percent was 31.71 when using four classes, 22.14 percent when
using five classes and 22.53 percent when using six classes. It was expected
that the classification would be poor when using four endmembers, as two
classes/endmembers was missing. Despite the poor classification, this is the
only image where it looks like the FCLS method successfully calculated the
fractional contribution for the endmembers on the scene. In the two other
classification results, using five and six endmembers, the nilas class (cyan
colour) are dominating. In figure 10.18 c, the ARE value is sharply decreasing
on the fifth endmember. The nilas endmember was extracted when the ATGP
algorithm was set to find five endmembers. Clearly there is a correlation
between these results.

Figure 10.20 to figure 10.23 shows how the abundance values were changed
when five or more endmembers got extracted. When three (figure 10.20)
and four (figure 10.21) endmembers were extracted, none of the abundances
dominated. The situation was not the same when five (figure 10.22) and six
(figure 10.23) endmembers was extracted. Then the abundance corresponding
to the nilas endmember dominated.

For the ARE results using the ATGP and the NFINDR endmembers, 10.15
and 10.18, all showed a sharp decrease in values on a given endmember

number. The behaviour for the corresponding abundances values are similar to the behaviour for the abundance values explained above. When the ARE value decrease sharply, one of the abundances corresponding to one of the endmembers dominates the system. It is like the system is over fitted/over trained. The linear mixing model is probably not sufficent when working with QUAD-POL data from sea ice scenes since, as the pixels most likely are nonlinearly mixed.

The synthetic data was made using the linear mixing model. All the samples in the synthetic data are therefore linearly mixed. The results for reconstructing the synthetic data was therefore much better than the reconstruction of the data consisting of nonlinear mixed pixels. Figure 10.24 shows the results of the ARE value using endmembers extracted from an synthetic dataset generated by using four classes. On these figures, the ARE value becomes really low when using four endmembers, which make sense since it is the number of classes the dataset consist of.

To illustrate that the reconstruction works on the linearly mixed synthetic data and does not contain the same issues as the mentioned nonlinearly mixed data, the distribution of each endmember in the scene have been calculated. This was conducted by locating how many samples each endmember had the largest contribution on. The results using four to six endmembers are shown in the histogram plots in figure 10.25. The figures shows that none of the endmembers are dominating the reconstruction as the form on the histogram are very uniform.
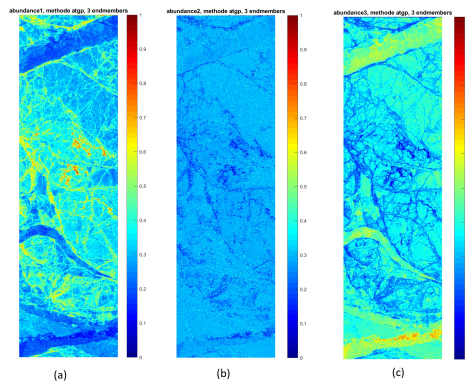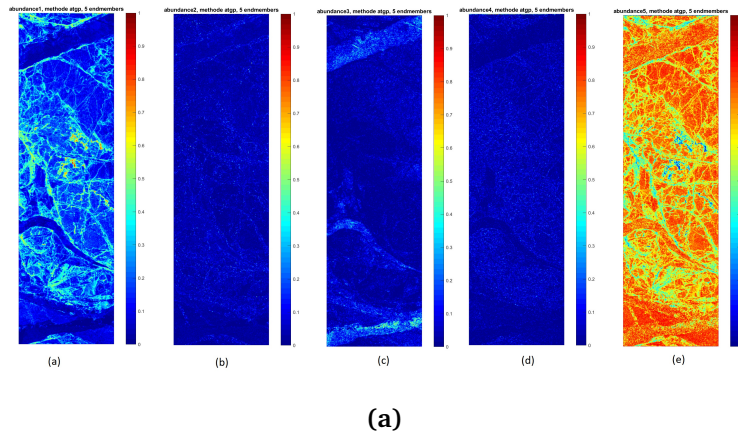
(a)

Figure 10.20: The figure shows the fractional contributions a endmember have to each pixels. Three endmembers were extracted using ATGP. Figure (a) shows the abundance of endmember one, figure (b) shows the abundance of endmember two and figure (c) shows the abundance of endmember three. Blue color indicates that the endmember has low contributions on the given pixel. Red colour indicates high contributions on each pixel.
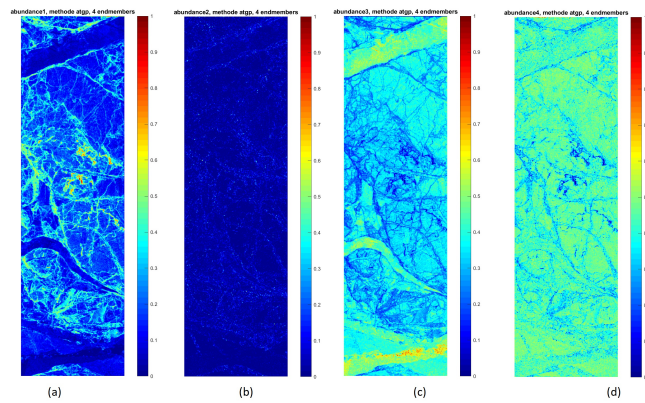
(a)

Figure 10.21: The figure shows the fractional contributions a endmember have to each pixels. Four endmembers were extracted using ATGP. Figure (a) shows the abundance of endmember one, figure (b) shows the abundance of endmember two, figure (c) shows the abundance of endmember three and figure (d) shows the abundance of endmember four. Blue color indicates that the endmember has low contributions on the given pixel. Red colour indicates high contributions on each pixel.
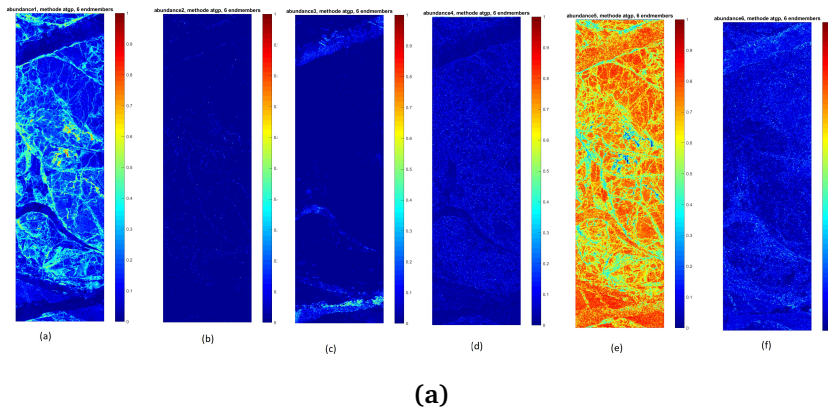
(a)

Figure 10.22: The figure shows the fractional contributions a endmember have to each pixels. Five endmembers were extracted using ATGP. Figure (a) shows the abundance of endmember one, figure (b) shows the abundance of endmember two, figure (c) shows the abundance of endmember three, figure (d) shows the abundance of endmember four and figure (e) shows the abundance of endmember five. Blue color indicates that the endmember has low contributions on the given pixel. Red colour indicates high contributions on each pixel


(a)

Figure 10.23: The figure shows the fractional contributions a endmember have to each pixels. Six endmembers were extracted using ATGP. Figure (a) shows the abundance of endmember one, figure (b) shows the abundance of endmember two, figure (c) shows the abundance of endmember three, figure (d) shows the abundance of endmember four, figure (e) shows the abundance of endmember five and figure (f) shows the abundance of endmember six. Blue color indicates that the endmember has low contributions on the given pixel. Red colour indicates high contributions on each pixel
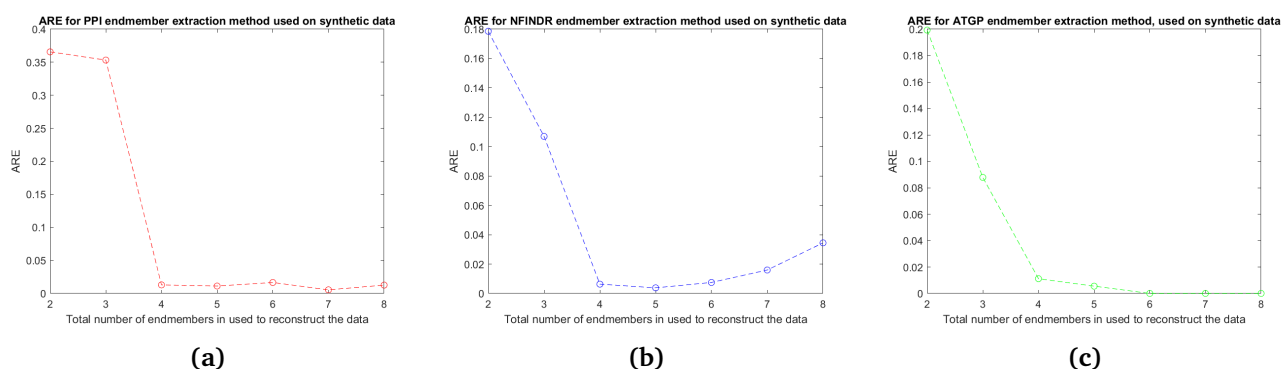
Figure 10.24: The ARE results on the reconstruction of synthetic dataset generated by using four endmembers. Figure (a) endmember extracted by using the PPI algorithm. Figure (b) endmember extracted by using the NFINDR algorithm. Figure (c) endmember extracted by using the ATGP algorithm.
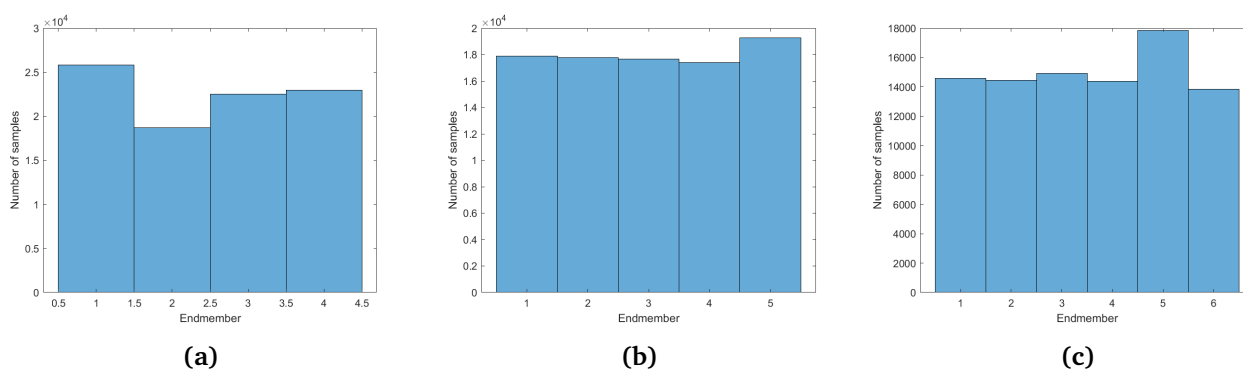
Figure 10.25: Histogram plot shows how many samples each endmember have the largest contribution on. The endmembers are extracted using the ATGP algorithm on the synthetic datasets. In figure (a) four endmembers was extracted from synthetic dataset which is generated by using four endmembers extracted from IceSAR data. In figure (b) five endmembers was extracted from synthetic dataset which is generated by using five endmembers extracted from IceSAR data. In figure (c) was six endmembers were extracted from synthetic dataset which is generated by using six endmembers extracted from IceSAR data

### 10.3.3 ARE, abundance and classification using nonlinear mixing model

A few experiments were also conducted using the bilinear mixing model. The results was better than the results using the linear mixing model, however still far from good enough. Figure 10.26 shows the ARE result using the bilinear

mixing model. The result were similar as to the ARE results using the linear mixing model. When using the nonlinear mixing model, the ARE value rapidly decreased on the fifth endmember.

Figure 10.27a shows the classification of the IceSAR data using six classes. By comparing this classification result with the classification result using the ROI separability method (figure 8.7c), we can see that the nonlinear classification method managed to separate open water, thin ice (nilas) and thicker ice from each other. The linear classification method did not manage to separate open water, thin ice and thicker ice from each other. The method only managed to separate thin ice from thick ice, and it didn't manage to separate thin ice from open water. Open water was classified as nilas when using the linear classification method.

When using the linear mixing model, the nilas class dominated the classification results. This is not the case when using the nonlinear mixing model. Figure 10.27b shows the abundance for the nilas endmember. By studying the figure we can see how the nilas endmember only contains high abundance value for the areas in the IceSAR scene which consist of nilas.

However, the nonlinear classification method didn't manage to separate the different thick ice classes (deformed ice, grey ice, grey white ice and level ice) from each other. The trouble in separating the classes was probably caused by the polarimetric features values being similar for the different thick ice classes. Another issue is that the system will not consider variability in the classes. This issue will be discussed further in the following subsection.
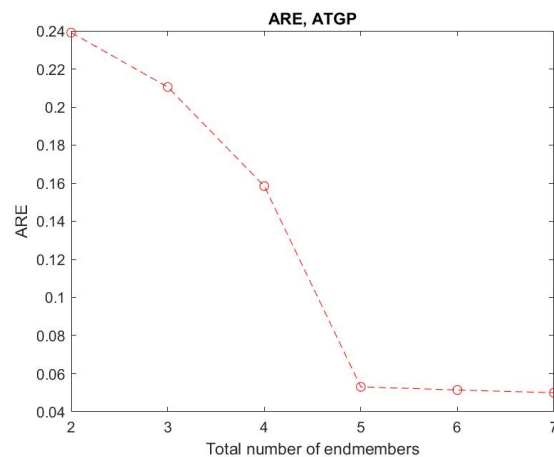
(a)

Figure 10.26: The figure shows the result of the ARE value of the IceSAR data when using the nonlinear unmixing.

(a)   **(b)**
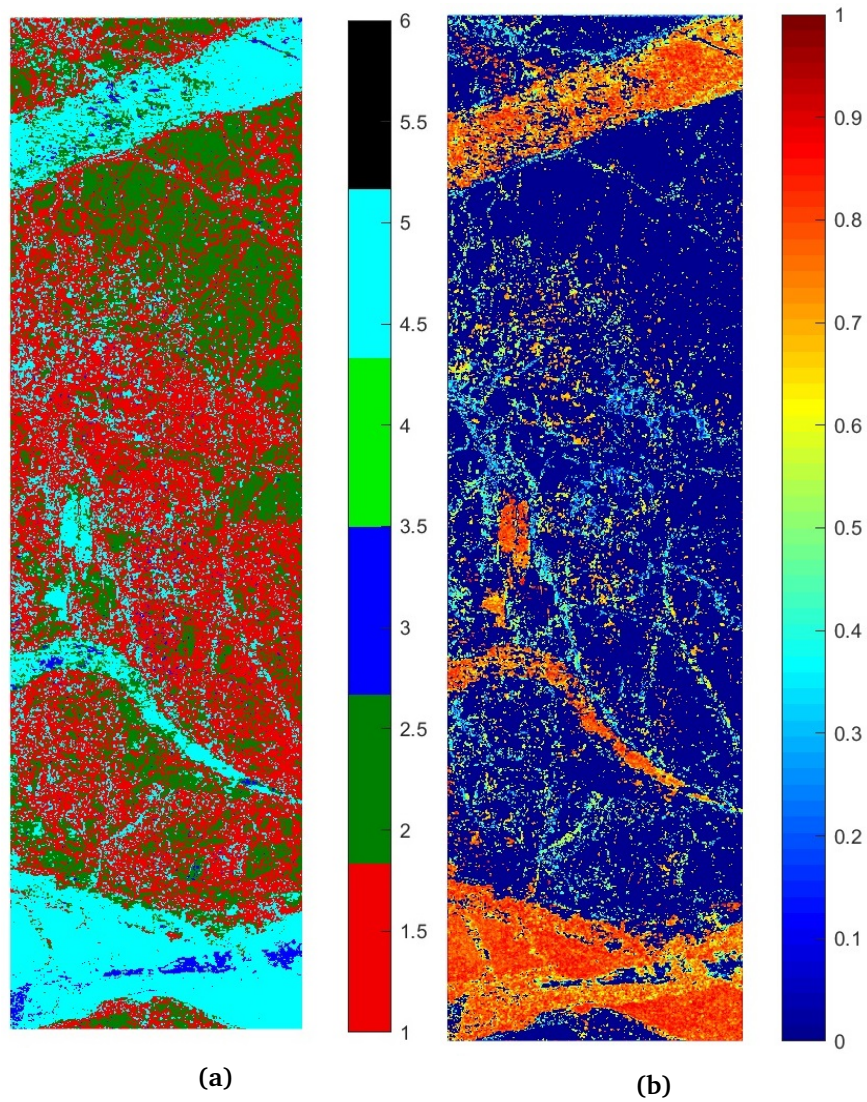
Figure 10.27: Figure (a) shows the classification using the bilinear mixing model on the IceSAR data. The classification have used six endmembers. Dark blue color is open water, light green is grey white ice, black is level ice, red is deformed ice, cyan is nilas and dark green is grey ice. Figure (b) shows the abundance values for the nilas endmember. Red color indicates strong abundance value while blue color indicates low abundance value.

10.3.4   Variability in the dataset

The reason for the system not being capable of estimating the abundances correctly for the real datasets, might have been caused by the system not being able to consider variability in the classes. Some of the classes may have

large variation in their polarimetric feature values. When the system is not considering the variation of classes, the system will face difficulty in separating the classes. Further, the polarimetric feature values for the different classes might have similar values compared to each other.

Combining these two scenarios, the resulting data manifold in the multidimensional feature space will be distributed in such a way that it is impossible for this approach to separate the classes properly. Figure 10.28 shows the distribution of the IceSAR data in a three-dimensional feature space. The different colours represent the different classes in the data. In the figure, the large variation in the classes polarimetric feature values is illustrated. Further, the figure illustrate how similar the polarimetric feature values are for the different classes. The system discussed in this thesis require a dataset with less variability in order to work. When generating the synthetic datasets, we get such a dataset.

(a)   **(b)**   **(c)**
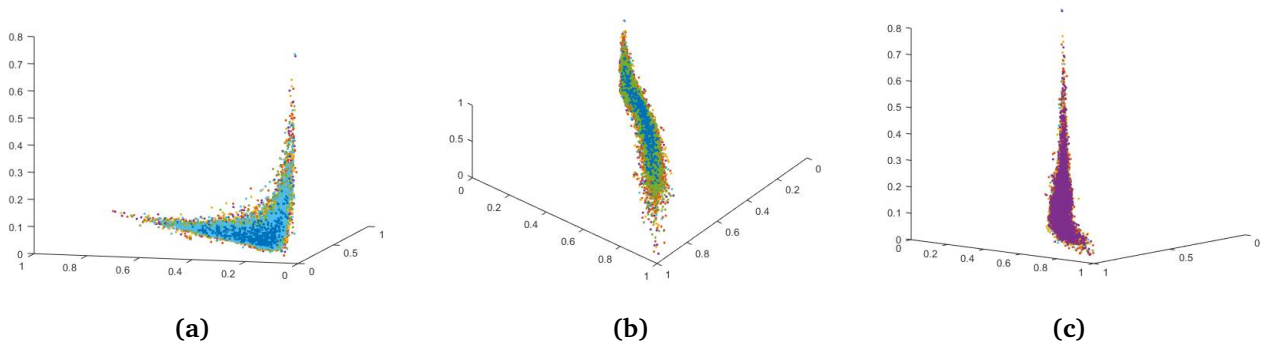
Figure 10.28: The figure shows the distribution of the IceSAR data in a three-dimensional feature space using three features. First feature is the first diagonal in the covariance matrix. The second feature is the first eigenvalue of the sample covariance matrix. Last feature is the pedestal height. (a), (b) and (c) represent different angles of the three-dimensional feature space.
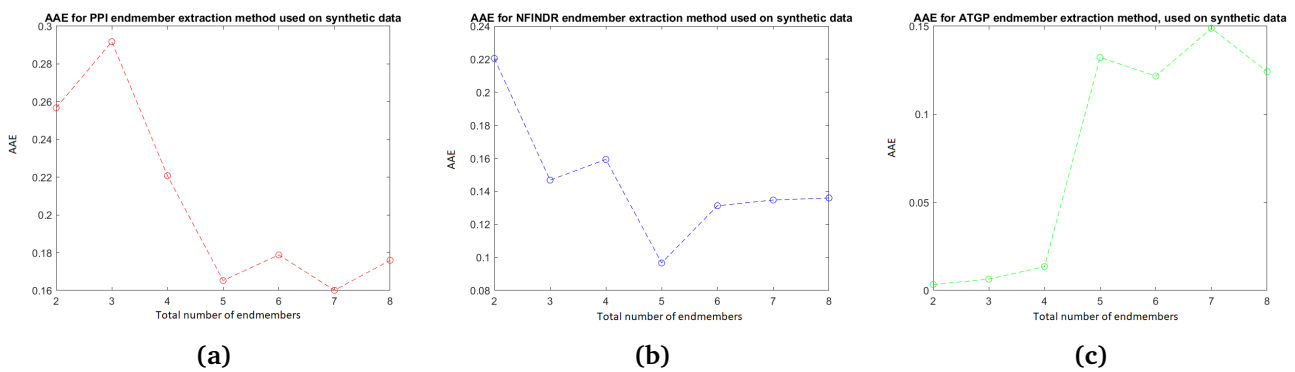
10.3.5 Abundance estimation

This sub section will focus on the ability of the FCLS method to estimate the abundance coefficients from a dataset.

By using the synthetic datasets and the AAE equation (equation 7.15), it is possible to obtain a validation on that. The results of calculating the AAE from the synthetic data, which was generated using endmembers from the IceSAR data, is shown in figure 10.29. One can see from the plots in the figure that the difference between the original abundance in the synthetic data and

the estimated abundance is small, meaning that the FCLS method have done a good job in estimating the abundances in the synthetic dataset. Still, the synthetic datasets do not have the same challenges as real sea ice datasets have. This will likely have a mayor impact on the positive result.

There are some variations in the AAE values in figure 10.29. These variations are correlated with the SNR in the dataset. Figure 9.3 shows the SNR. For different number of endmembers in the dataset, there are different values of SNR. When the SNR is high, the AAE value is low. It is opposite when the SNR is low. The AAE value is then high

(a)   **(b)**   **(c)**

Figure 10.29: AAE results for abundance estimation of the synthetic dataset generated by using endmembers from IceSAR data. Figure (a): endmembers extracted by using the PPI algorithm. Figure (b): endmembers extracted by using the NFINDR algorithm. Figure (c): endmembers extracted by using ATGP algorithm

/11

Conclusion

The aim of the work in this thesis was to explore a new system for enhancing the characterization of earth surface by means of SAR image analysis. Traditionally, target decomposition approaches has used the scattering space. In this thesis the approach has been used to explore the feature space associated with the covariance matrix-based features which is computed from QUAD-POL signals. To properly and efficiently do so, several steps has been taken.

The first step was generating multidimensional datasets using nine different features, which all were computed using the covariance matrix. This was done on the Radarsat2, the ALOS2 and the IceSAR datasets. All the datasets contained sea ice scenes. The next step in the approach was to extract the endmembers from the datasets. To extract the endmembers, the PPI, the NFINDR and the ATGP algorithms where used. These endmembers were used, together with the theory for a linear mixing model, to generate synthetic datasets. By generating synthetic datasets, an additional review of the approach was conducted. The OEN method was introduced to this approach to provide information on the number of classes the scenes consisted of. The last step in the approach was to unmix the data. By doing this we would get information on how much each class are representing a given pixel of the earth surface scene. Unmixing was conducted using both the linear and bilinear mixing models. The FCLS method was used in order to estimate the abundance coefficients.

In order to validate the approach used in this thesis, several steps have been tested and conducted. Each sea ice dataset included a ground truth. These

ground truth datasets had one of the key parts in validating the approach and the different steps in it. The results using the endmember extraction algorithms was analysed using these ground truths, which made it possible to validate if the algorithms were capable to find different pure pixels in the scene. To review the performance of the OEN method, both the ground truth datasets and the synthetic datasets was utilized. The synthetic datasets could be used for this, as we always knew the number of classes in these datasets. To obtain a validation on the correctness of the unmixing results, additional methods where done. The methods were as follows: Reconstruction of the data, calculation of the ARE and the AAE, classification of the IceSAR data, studding the abundance coefficients values and pixel error reconstruction .

The performance using the different endmember extraction algorithms was not equal and not all the algorithms gave brilliant results. The NFINDR and ATGP algorithms worked very well as they managed to locate different pure pixels in the scenes. The PPI algorithm did not provide equally good results as it was only capable of locating open water, thicker ice and thinner ice. Accordingly, all further experiments using the endmembers extracted by the PPI algorithm resulted in strange and poor results.

None of the results using any of the endmember extraction algorithms was successful when using the ground truth belonging to the Radarsat2 dataset. This is because the distribution of the ice thickness was gamma distributed.

Most of the results using the OEN method was successful, especially when using it on the synthetic data. However, when the method was tested on real sea ice data, it would sometimes miss with one class. This was probably caused by the distribution and shape of the data manifold.

The unmixing results on the sea ice data was poor. When using the linear mixing model and the suggested number of endmembers, which was successfully calculated using the OEN method, one of the endmembers always dominated the unmixing results. The classification, ARE and the abundance results confirmed it. When using the bilinear mixing model, non of the endmembers dominated the unmixing results, but the approach were not capable to separate the different classes of thick sea ice.

On the other hand, the unmixing results on the synthetic dataset proved to be very successful as none of the endmembers dominated the unmixing results. This was proved by calculating the number of samples each endmember had the largest contribution on. The results were uniformly distributed.

The approach in this thesis do not consider variability for the polarimetric feature values in the different classes. For most of the conducted experiments,

it also assumes that the pixels are linearly mixed, something they probably not are, especially for the sea ice data. As a consequence, the approach is not able to retrieve accurate and reliable estimates on the earth composition for scenes consisting of sea ice. However, this approach has given good results on dataset not suffering from these challenges.

This project has some limitations. First, the number of skewers was only set to 1000 when using the PPI algorithm. Increasing the number of skewers would probably have resulted in better results using the algorithm. Still, the computational cost increased drastically when this was tested. The other limitations where due to the different ground truths. As mentioned earlier, it was not possible to use the ground truth belonging to the Radarsat2 dataset because of the distribution of the ice thickness. The use of the ALOS2 ground truth was very limited because it was not possible to differ between more than three classes when using this ground truth. Also, since there is some difference in time for when the two datasets were acquired, there can be changes in the scenery due to sea ice drift. Further, eye vision was used to classify the endmembers by comparing the intensity image and the corresponding optical image, accordingly there are no guaranties for the classification being correct. The ground truth belonging to the IceSAR data is limited as it is made from the ROI separability method. There is no guaranty that the classification using the ROI separability method is correct for all the samples.

Further work on this thesis and its approach would be adapting the approach in such a way that it considers the variability sea ice data suffers from. As the methods for linear mixing did not work as intended, it should be replaced with methods for nonlinear mixing. The bilinear mixing model didn't return perfectly unmixing results either. Still, only one bilinear mixing model (equation 3.3) were investigated in this thesis. There exist several other bilinear mixing models which could be tested in further research on the given issues of this thesis.

References

Abid Jamal, E. l. (2017). *Difference between monostatic radar and bistatic radar.* `https://www.electronicslovers.com/2017/05/difference-between-monostatic-radar.html`. (Accessed: 15-03-2019)

Bhattacharya, S., Blumensath, T., Mulgrew, B., & Davies, M. (2007). Fast encoding of synthetic aperture radar raw data using compressed sensing. In *2007 ieee/sp 14th workshop on statistical signal processing* (pp. 448–452).

Bioucas-Dias, J. M., Plaza, A., Dobigeon, N., Parente, M., Du, Q., Gader, P., & Chanussot, J. (2012). Hyperspectral unmixing overview: Geometrical, statistical, and sparse regression-based approaches. *IEEE journal of selected topics in applied earth observations and remote sensing, 5*(2), 354–379.

Campbell, J. B., & Wynne, R. H. (2011). *Introduction to remote sensing.* Guilford Press.

Çetin, M., & Karl, W. C. (2001). Feature-enhanced synthetic aperture radar image formation based on nonquadratic regularization. *IEEE Transactions on Image Processing, 10*(4), 623–631.

Chang, C.-I., Zhao, X.-L., Althouse, M. L., & Pan, J. J. (1998). Least squares subspace projection approach to mixed pixel classification for hyperspectral images. *IEEE Transactions on Geoscience and Remote Sensing, 36*(3), 898–912.

Chapron, P. B. (2012). *Sar.* `http://solab.rshu.ru/media/1115/SAR_28March2012_final.pdf`. (Accessed: 23-03-2019)

CRISP. (2001a). *Microwave bands.* `https://crisp.nus.edu.sg/~research/tutorial/freqpol.htm`. (Accessed: 23-03-2019)

CRISP. (2001b). *Sar principal.* `https://crisp.nus.edu.sg/~research/tutorial/mw.htm`. (Accessed: 15-03-2019)

Danielsen, D. N. (2018). Multidimensional analysis of polsar images. , 10-12. (not published)

Dobigeon, N., Tourneret, J.-Y., Richard, C., Bermudez, J. C. M., McLaughlin, S., & Hero, A. O. (2014). Nonlinear unmixing of hyperspectral images: Models and algorithms. *IEEE Signal Processing Magazine, 31*(1), 82–94.

Elachi, C., & Van Zyl, J. J. (2006). *Introduction to the physics and techniques of remote sensing* (Vol. 28). John Wiley & Sons.

ESA, E. (2009). *Radar basic.* `https://earth.esa.int/landtraining09/`

`D1La1_Halounova_SARBasics.pdf`. (Accessed: 23-03-2019)

ESA, E. (2014a). *Geometry glossary*. `https://earth.esa.int/handbooks/`
`asar/CNTR5-5.html`. (Accessed: 07-12-2018)

ESA, E. (2014b). *Radar and sar glossary*. `https://earth.esa.int/`
`handbooks/asar/CNTR5-2.html#eph.asar.gloss.radsar:`
`ACTIVE_SYSTEM`. (Accessed: 08-12-2018)

ESA, E. (2014c). *Sar*. `https://earth.esa.int/web/guest/missions/esa`
`-operational-eo-missions/ers/instruments/sar/applications/`
`radar-courses/content-2/-/asset_publisher/qIBc6NYRXfnG/`
`content/radar-course-2-synthetic-aperture-radar`. (Accessed:
23-03-2019)

ESA, E. (2019). *Radar equation*. `https://earth.esa.int/`
`web/guest/missions/esa-operational-eo-missions/`
`ers/instruments/sar/applications/radar-courses/`
`content-2/-/asset_publisher/qIBc6NYRXfnG/content/`
`radar-course-3-the-radar-equation;jsessionid=`
`4D31A230B818C6634AE68D9E8EA2440C.jvm1?redirect=https%`
`3A%2F%2Fearth.esa.int%2Fweb%2Fguest%2Fmissions%2Fesa`
`-operational-eo-missions%2Fers%2Finstruments%2Fsar%`
`2Fapplications%2Fradar-courses%2Fcontent-2%3Bjsessionid%`
`3D4D31A230B818C6634AE68D9E8EA2440C.jvm1%3Fp_p_id%3D101`
`_INSTANCE_qIBc6NYRXfnG%26p_p_lifecycle%3D0%26p_p_state%`
`3Dnormal%26p_p_mode%3Dview%26p_p_col_id%3Dcolumn-1%26p_p`
`_col_count%3D1`. (Accessed: 25-03-2019)

Esmaeilzade, M., Jahani, F., & Amini, J. (2017). Using covariance matrix for
change detection of polarimetric sar data. *ISPRS-International Archives
of the Photogrammetry, Remote Sensing and Spatial Information Sciences*,
69–76.

Facility, A. S. (n.d.). *Radar and sar glossary*. `https://www.asf.alaska.edu/`
`asf-tutorials/sar-basics/`. (Accessed: 07-12-2018)

Hapke, B. (2012). *Theory of reflectance and emittance spectroscopy*. Cambridge
university press.

Harris. (2018). *Hyperspectral imaging: An emerging tool for mission readiness*. `https://www.harris.com/perspectives/`
`global-situational-awareness/hyperspectral-imaging-an`
`-emerging-tool-for-mission`. (Accessed: 18-02-2019)

Harsanyi, J. C., & Chang, C.-I. (1994). Hyperspectral image classification and
dimensionality reduction: An orthogonal subspace projection approach.
IEEE Transactions on geoscience and remote sensing, 32(4), 779–785.

Heinz, D. C., et al. (2001). Fully constrained least squares linear spectral
mixture analysis method for material quantification in hyperspectral
imagery. *IEEE transactions on geoscience and remote sensing, 39*(3), 529–
545.

Heylen, R., Burazerovic, D., & Scheunders, P. (2011). Non-linear spectral

unmixing by geodesic simplex volume maximization. *IEEE Journal of Selected Topics in Signal Processing, 5*(3), 534–542.

Heylen, R., Parente, M., & Gader, P. (2014). A review of nonlinear hyperspectral unmixing methods. *IEEE Journal of Selected Topics in Applied Earth Observations and Remote Sensing, 7*(6), 1844–1868.

Jelínková, H. (2013). *Lasers for medical applications: diagnostics, therapy and surgery*. Elsevier.

Kersten, P. R., Lee, J.-S., & Ainsworth, T. L. (2005). Unsupervised classification of polarimetric synthetic aperture radar images using fuzzy clustering and em clustering. *IEEE Transactions on Geoscience and Remote Sensing, 43*(3), 519–527.

Lee, J.-S., & Pottier, E. (2009). *Polarimetric radar imaging: from basics to applications*. CRC press.

Maitra, S., Gartley, M. G., Faulring, J., & Kerekes, J. P. (2013). Characterization of basic scattering mechanisms using laboratory based polarimetric synthetic aperture radar imaging. In *2013 ieee international geoscience and remote sensing symposium-igarss* (pp. 4479–4482).

Maitra, S., Gartley, M. G., Faulring, J., & Kerekes, J. P. (2013, July). Characterization of basic scattering mechanisms using laboratory based polarimetric synthetic aperture radar imaging. In *2013 ieee international geoscience and remote sensing symposium - igarss* (p. 4479-4482). doi: 10.1109/IGARSS.2013.6723830

MDA. (2015). *Radarsat-2 imaging modes and applications.* https://mdacorporation.com/docs/default-source/brochures/geospatial-services/webinar---radarsat-2-imaging-modes-and-applications.pdf?sfvrsn=2. (Accessed: 13-04-2019)

NASDA, N. S. D. A. O. J. (1996a). *Surface scattering.* http://wtlab.iis.u-tokyo.ac.jp/wataru/lecture/rsgis/rsnote/cp3/cp3-4.htm. (Accessed: 27-03-2019)

NASDA, N. S. D. A. O. J. (1996b). *Volume scattering.* http://wtlab.iis.u-tokyo.ac.jp/wataru/lecture/rsgis/rsnote/cp3/cp3-5.htm. (Accessed: 27-03-2019)

Natural Resources Canada, N. (2015). *Radar polarimetry.* https://www.nrcan.gc.ca/earth-sciences/geomatics/satellite-imagery-air-photos/satellite-imagery-products/educational-resources/9275. (Accessed: 16-05-2019)

Plaza, A., Martinez, P., Pérez, R., & Plaza, J. (2002). Spatial/spectral endmember extraction by multidimensional morphological operations. *IEEE transactions on geoscience and remote sensing, 40*(9), 2025–2041.

Podest, E. (2017). *Basics of synthetic aperture radar.* https://arset.gsfc.nasa.gov/sites/default/files/water/Brazil_2017/Day1/S1P2.pdf. (Accessed: 23-03-2019)

Puschner. (n.d.). *Penetration depth.* http://www.pueschner.com/en/microwave-technology/penetration-depths. (Accessed: 27-03-

2019)

Research, C. F. S. (n.d.). *Analysis methods for sar data.* `http://www.csr`
`.utexas.edu/projects/rs/whatissar/analysis.html`. (Accessed:
27-03-2019)

Rizzoli, P., & Brautigam, B. (2014). Radar backscatter modeling based on
global tandem-x mission data. *IEEE Transactions on Geoscience and
Remote Sensing, 52*(9), 5974–5988.

Settle, J., & Drake, N. (1993). Linear mixing and the estimation of ground cover
proportions. *International Journal of Remote Sensing, 14*(6), 1159–1177.

Tu, T.-M., Chen, C.-H., & Chang, C.-I. (1997). A posteriori least squares
orthogonal subspace projection approach to desired signature extraction
and detection. *IEEE Transactions on geoscience and remote sensing, 35*(1),
127–139.

Tutorialspoint. (n.d.). *Radar equation.* `https://www.tutorialspoint`
`.com/radar_systems/radar_systems_range_equation.htm`, note =
Accessed: 12-03-2019.

USGS. (n.d.). *Microwave bands.* `https://www.usgs.gov/centers/`
`eros/science/usgs-eros-archive-radar-synthetic-aperture`
`-radar-sar-processing-system?qt-science_center_objects=0#`
`qt-science_center_objects`. (Accessed: 23-03-2019)

Wikipedia. (2019a). *Lambertian reflectance.* `https://en.wikipedia.org/`
`wiki/Lambertian_reflectance`. (Accessed: 27-03-2019)

Wikipedia. (2019b). *Microwave bands.* `https://en.wikipedia.org/wiki/`
`Microwave#/media/File:Atmospheric_electromagnetic_opacity`
`.svg`. (Accessed: 23-03-2019)

wolfram, M. (n.d.). *Complex number.* `http://mathworld.wolfram.com/`
`ComplexNumber.html`. (Accessed: 21-11-2018)